FOCAL FIELD DISTRIBUTIONS FOR CYLINDRICAL VECTOR BEAMS: ANTI-RESOLUTION

WAN CHAO

(B. ENG., NATIONAL UNIVERSITY OF DEFENSE TECHNOLOGY, P.R.C)

A THESIS SUBMITTED FOR THE DEGREE OF DOCTOR OF PHILOSOPHY

DEPARTMENT OF ELECTRICAL AND COMPUTER ENGINEERING

NATIONAL UNIVERSITY OF SINGAPORE

2013

DECLARATION

I hereby declare that the thesis is my original work and it has been written by me in its entirety. I have duly acknowledged all the sources of information which have been used in the thesis.

This thesis has also not been submitted for any degree in any university previously.

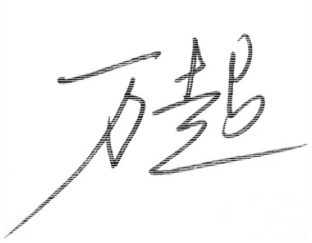

WAN CHAO

06 May 2013

Acknowledgements

I would like to take this opportunity to thank all the professors, teachers, friends and group members who have helped me make this thesis possible. I also appreciate the China Scholarship Council (CSC) for providing me the great opportunity to study in Singapore and offering the financial support for my study in the past four years.

First, I would like to send my warmest thanks to my supervisors Professor Qiu Chengwei and Professor Yeo Tatsoon for their guidance, supports, encouragement and kindness throughout my program. Their mentorship was paramount in providing a well-rounded experience consistent my long-term career goals.

I am indebted to these teachers and friends who have supported me a lot and greatly encouraged me when I was in the most difficult time: Professors Aaron J. Danner and Guo Yongxin from National University of Singapore, Professors Mao Junjie and Chai Shunlian from National University of Defense Technology, Professor Ding Weiqiang from Harbin Institude of Technogogy,

Mr. Fan Lijie, Mr. Tang Xingji and Dr. Peng Da from National University of Defense Technology.

Additionally, I am very grateful for the friendship of all of the members in microwave group: Dr. Huang Kun, Dr. Han Tiancheng, Dr. Zhang Lei, Mr. Ye Huapeng, Dr. Gao Dongliang, Dr. Duan Zhu, Dr. Sun Hucheng, Mr. Long Yunshen, Dr. Bao Xiaoyue, Miss Xu Lijie, and Miss Ren Rui. Thank you for your assistance and encouragements during my days in National University of Singapore.

Finally and most importantly, I am tremendously grateful for my parents. Their understanding and love encourage me to work hard and to continue pursuing a Ph.D. degree abroad. Their firm and dedicate personality has affected me to be steadfast and never bend to difficulty. I would like to thank my girlfriend, Miss Hua Zhilei. Her support, encouragement, quiet patience and unwavering love were undeniably the bedrock upon my past days.

Abstract

The tight focusing of cylindrical vector (CV) beams is widely used in real-world applications, such as particle manipulation, optical tweezers, and laser writing. As one of the most challenging topics in modern optics, the generation of a tight spot to achieve super-resolution imaging has been realized by focusing CV beams on the subwavelength scale. Generally, all the approaches reported in the literature manipulate the point spread function (PSF) to achieve a sharp PSF in the focal region. Interestingly, the exact opposite of super-resolution, i.e., suppressing the main lobe in the PSF until it has completely vanished and subsequently elevating the side lobe, remains an unexplored topic. For this inversely manipulated PSF, a point source at the object plane leads to a large-radius ring intensity, resulting in unresolved imaging at the imaging plane. This new scheme is defined in our concept as anti-resolution (AR). Contrary to the traditional PSF, which has been developed over the course of centuries, the concept of AR provides a new direction in manipulating the PSF and may lead to considerable discoveries in

physics.

The aim of this thesis was to model, characterize, and realize such AR using a binary optical system through an investigation of the energy flux of the light, light-matter interaction, and phase modulation mechanism. The electromagnetic null field, corresponding to AR, was created by optimizing the parameters of a binary optical element (BOE). When there is no energy on the optical axis as the PSF is fully suppressed, AR can be realized. It was determined that the null field region has a remarkably large volume of smeared-out PSF. In addition, the light intensity inside this volume is thoroughly diminished. These extraordinary findings strongly suggest a possible application of AR in the recently highlighted field of cloaking. Therefore, another aim of this thesis was to realize an AR-based cloaking method. The experimental design, cloaking mechanism, and cloaking performance were simultaneously investigated.

In conclusion, this study established a novel account of the manipulation of the optical beam and further employed this mechanism in macroscopic cloaking. As the mechanism is fully developed for the first time, other special manipulation techniques of vector beams can readily be further investigated based on this study. Meanwhile, this new concept of AR greatly enriches optical focusing and provides an unprecedented platform to focus light at the subwavelength scale. Moreover, this study provides a practical means of cloaking because several problems in previous cloaking methods, such as

bandwidth, polarization and fabrication, are overcome.

Contents

List of Figures

Chapter 1

Introduction

Light, a form of electromagnetic wave, is rigorously governed by Maxwell's equations. Studies on the intrinsic properties of light, such as the frequency, amplitude，phase and polarization, have laid the foundation for modern optics. For example, the attempt to control the frequency of light led to the birth of non-linear optics [1] and laser physics [2]. The manipulation of the amplitude and phase of light facilitated the emergence of micro-optics and diffractive optics [3]. As one of the basic properties of light, polarization is of crucial importance in theoretical descriptions and practical applications [4, 5]. Many applications, such as advanced imaging systems, inspection and metrology, high-intensity data storage, optical communications and material science, have greatly benefited from this vectorial property.

1.1 Objectives and significance

Until the early 1970s, researchers mainly focused on spatially homogeneous light polarization (shown in Figure 1.1a), whereby the polarization state does not depend on the location in the light cross section, such as for linear and circular polarizations [6]. Recently, cylindrical vector (CV) beams with spatially varying states of polarization (shown in Figure 1.1b) have been achieved in experiments [6, 7]. As a result, a large number of specific effects and phenomena have been observed and detected accordingly by tightly focusing these CV beams.

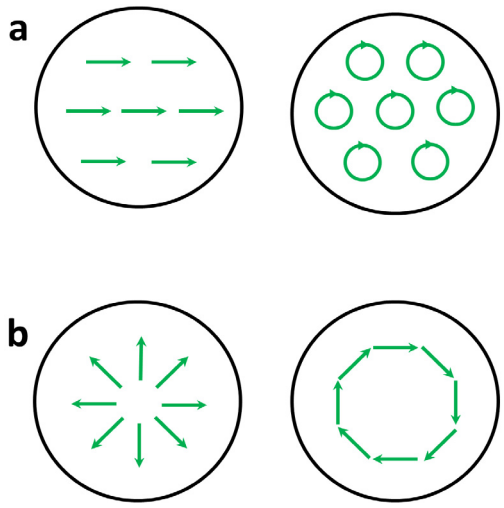

Figure 1.1. Spatially homogeneous and inhomogeneous polarization beams. (a) Cross sections of a linearly and a circularly polarized beam. (b) Cross sections of a radially and an azimuthally polarized beam.

Remarkably, simulations and experiments have confirmed that a tighter spot than that produced by spatially homogeneous polarizations can be achieved by focusing a radially polarized light beam (a type of CV beam) in a

high numerical (NA) aperture system. This discovery is of considerable importance to improve the lateral resolution of an optical system, and the principle behind this is the existence of a strong longitudinal field component in the adjacent region of the focus [8-11]. This crucial finding has aroused intensive concern within the academic community. Thus, much research effort has been dedicated to focusing the CV beams at the subwavelength scale to achieve super-resolution and to beat the diffraction limit [8, 9].

In the seminal study by S. Quabis et al. [8], the Hertzian dipole model was introduced to investigate the focusing properties of CV beams in the focal region. The limit of the spot size of the focused beams was proposed for the first time. As a pioneering attempt, this study comprehensively reveals the reason why a tighter spot could be achieved by focusing a radially polarized beam instead of a linearly polarized beam. Moreover, the main reason that the shape of the focus was affected was identified. Nevertheless, the explanations for the limit of the spot size of the focused beams are a lack of specifications. In addition, the effects of the longitudinal electric field on the focal shape are merely qualitatively described. Following the study by S. Quabis et al., the focusing property of a generalized CV beam was investigated by Zhan et al. [12]. They theoretically confirmed the spatial separation between the transverse and longitudinal components in the vicinity of the focus. Additionally, a focus of a flattop shape was realized by employing a polarization rotator. This study is particularly meaningful to other studies and

directly leads to the breakthrough of the experimental realization of a tighter spot in the focal region.

In addition to these theoretical discussions about high spatial resolution, the experimental verification of the longitudinal field in the focal region is an important step forward. In a novel experiment by L. Novotny et al. [13], the focal field distribution was probed by single molecules. It was found that the field strength ratio between longitudinal and transverse components is about two, which is in high agreement with the theoretical model. As a consequence, the existence of the longitudinal field was convincingly evidenced. Based on these substantial findings, R. Dorn et al. proposed a novel scheme of super-resolution by focusing a radially polarized beam with an annular aperture [9]. It was found that the spot size could be as small as $0.16\lambda^2$. This study has verified the prediction of the Hertzian dipole model, and it has a significant impact on improving the spatial resolution. Moreover, it paves the way for consequent studies, e.g., longitudinal optical needle for electron accelerator physics [14] and three-dimensional optical chain for particle delivery [15]. Such annular aperture can be replaced with a binary optical element (BOE) [16, 17]. In a recent work, an ultra-long optical needle has been realized by employing the electric dipole array radiation model, and the full-width at half maximum (FWHM) spot size in air is only $0.129\lambda^2$. However, the spot size limit predicted by Hertzian dipole model is not yet broken [17].

Following these fundamental studies in conventional optics, other

strategies have also been proposed to reduce the spot size, such as using superlenses [18] and hyperlenses [19]. Concurrently, significant effort concerning optical super-resolution has been devoted to the development of various optical microscopy techniques (e.g., stimulated emission depletion microscopy [20] and stochastic optical reconstruction microscopy [21]) based on molecular labeling, nonlinear optical saturation, luminescence, and the excitation/ de-excitation of fluorophores.

It is well known that the point spread function (PSF) (Figure 1.2a) dictates the performance of an optical focusing system [22, 23], so a sharp PSF with a strong main lobe and a weak side lobe (Figure 1.2b) is highly desired for realizing high spatial resolution [24, 25]. From this point of view, all the studies mentioned above, no matter what type of scheme they have adopted, have one thing in common: their final target is to narrow down the PSF.

One interesting question beyond the current focus is what new interesting phenomena and applications would exist if one pushes the limit toward the other extreme, i.e., suppressing and flattening the main lobe in the PSF until it has completely vanished, and increasing the sidelobe (Figure 1.2d), which is completely opposite of the technique of super-resolution in Figure 1.2b. For this inversely manipulated PSF, a point source at the object plane leads to a large-radius ring intensity, resulting in the dis-resolved imaging at the imaging plane. This new scheme is defined in our concept as anti-resolution (AR). In

contrast to the traditional PSF, which has been investigated for centuries, AR provides a new direction to manipulate the PSF and extends the concept of the PSF to a broader range. Moreover, this scheme indicates many considerable discoveries and applications in optics and physics. In view of the above reasons, the main aim of this thesis was to model, characterize, and realize such AR in a binary optical system (Figure 1.2e). The energy flux of the light, light-matter interaction, and phase modulation mechanism were investigated as specific objectives.

The phenomenon of AR may have significant impact on the development of an effective methodology to manipulate optical beams, and will undoubtedly extend the practical applications of focusing optics. Because the mechanism of AR is comprehensively revealed, other novel phenomena of CV beams can be readily investigated following this study. Meanwhile, the new concept of AR-focusing optics may provide an alternative platform to focus light on subwavelength scale.

In this study, AR only denotes the inverse manipulation of the PSF in contrast with that of the PSF for super-resolution (refer to Figures 1.2b and 1.2d), and it has a relocated PSF with a ring-shaped intensity distribution. This implementation creates a macroscopic spatial region with a nearly perfect electromagnetic null field, where the energy flux of light approaches zero. The electromagnetic null field in the PSF spreads in the focal region, producing a uniform variation in the energy flux in the homogenous medium, resulting in a

large null-field region surrounded by visible light, which looks like a three-dimensional "optical capsule" (Figure 1.2f). Additionally, the AR phenomenon has a similar energy flex with the invisibility cloak, a device that can make an object invisible (Figure 1.3).

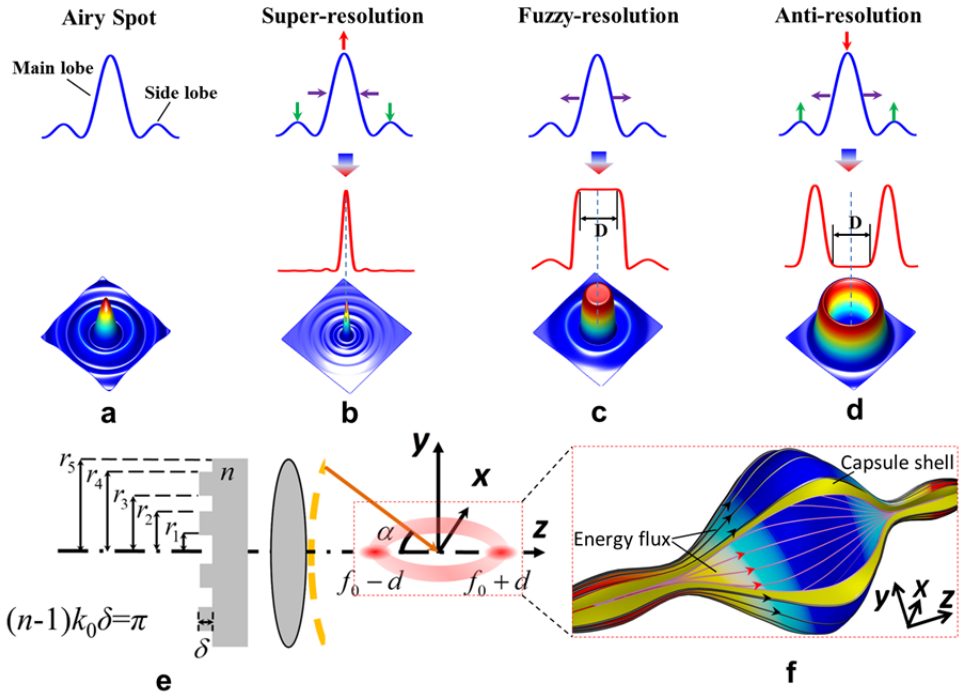

Figure 1.2. Evolution from super-resolution to anti-resolution (AR) [Appendix B 1]. The PSF of a traditional optical imaging system has the form of Airy spot (a). The super-resolution in (b) is achieved by narrowing the PSF, enhancing the main lobe as well as suppressing the side lobe. If we just widen the PSF without any disposing of main lobe and side lobe in PSF, the fuzzy-resolution (c) leading to degradation in imaging can be obtained. One completely inverse case of (b) in manipulation of PSF is widening the PSF, suppressing the main lobe and enhancing the side lobe so that the PSF in the region D (>> λ) completely vanishes, which is the concept of AR (d). (e) The scheme for realizing visible light capsule based on AR with binary phase on. (f) The 3D optical capsule based on AR concept. Energy flows in the capsule whose outer and inner boundaries are shown by the black and red curves, respectively.

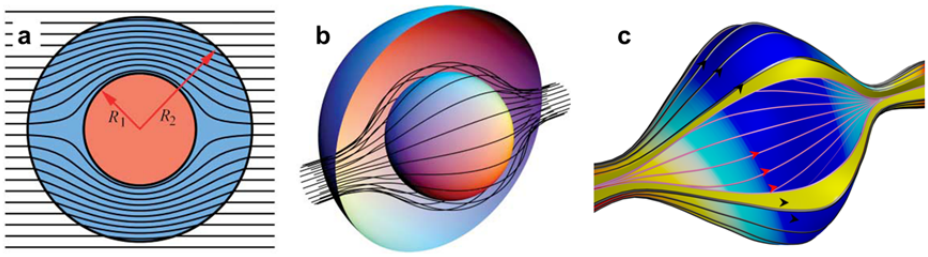

Figure 1.3. Invisibility cloak and AR phenomenon. (a) A two-dimentional cross section of the cloak. (b) A three-dimentional cross section of the cloak. (c) The AR phenomenon. (a) and (b) are reprinted from [26]. Reprinted with permission from AAAS.

These extraordinary results strongly suggest a possible application of AR in the recently highlighted area of cloaking. Therefore, another aim of this thesis was to realize AR-based cloaking. The experimental design, cloaking mechanism, and cloaking preformace were therefore investigated. The AR-based cloaking is of considerable importance in realistic applications because the anisotropic materials and inhomogeneous structures, which are required by traditional cloaking methodologies, are not necessary for the proposed scheme.

1.2 Thesis plan

To achieve the phenomenon of AR and AR-based cloaking, we divide this study into three parts: the theoretical modeling, AR phenomenon realization and experimental verification. These three parts are interrelated and contribute to the final results in a logical manner.

The main text of the thesis starts with a discussion of the background studies behind this research. Subsequently, the phenomenon of AR and its

concept are properly defined, followed by an emphasis on the objectives and the significance of this study.

The mathematical foundations of the CV beam are derived in Chapter 2. The general expression for the CV beam, which includes the radial and azimuthal components, is discussed. To further investigate the electromagnetic field distribution in the focal region of an aplanatic imaging system, the Debye integral is employed and derived to provide an approximated description, resulting in the Richards-Wolf's formula that is widely used in the high-NA imaging system. This chapter provides the theoretical basis for the novel phenomena of AR.

Chapter 3 is used to introduce this new phenomenon, AR PSF, which is created using a BOE and a focusing lens (Figure 1.2e). In addition, we further investigate the physical properties of the AR PSF by varying the parameters of the BOE and the polarization of the incident light. It is found that the volume of the electromagnetic null field induced by the AR PSF is tunable. This demonstrates its great flexibility and universal properties for various imaging systems. Subsequently, an algorithm used for the design of BOE is proposed and employed to investigate the underlying physics of the AR phenomenon.

Based on the results in Chapter 2 and Chapter 3, we apply the phenomenon of AR to optical cloaking in an imaging system in Chapter 4. In the simulation, we demonstrate the energy flow of the light and discuss the relation between the volume of the cloaked region and the lens NA. Next, two

well-designed experiments are implemented to verify the feasibility of the cloaking technique.

Finally, a conclusion of this thesis is provided as a summary of this work. Based on personal knowledge in this field, some suggestions are also provided for further research by extending the reported results to other related fields.

Through the work we have performed, the phenomenon of AR is theoretically and experimentally demonstrated. It is further shown that a null field with nearly zero-field intensity is surrounded by light and that this null-field area is up to eight orders of magnitude larger than λ^2 in cross-sectional size. Based on this novel phenomenon, an optical cloak is proposed and experimentally demonstrated. This cloak functions very well using arbitrarily polarized beams in three dimensions, and is also frequency scalable over the whole electromagnetic spectrum.

Chapter 2

Theoretical background for cylindrical vector beams

2.1 Maxwell's equations

The laws of electricity and magnetism were discovered by James Clerk Maxwell (1831-1879) in 1873 [27-34]. They are given in differential form as

$$\nabla \times \boldsymbol{E} = -\frac{\partial}{\partial t}\boldsymbol{B}, \tag{2.1}$$

$$\nabla \times \boldsymbol{H} = \frac{\partial}{\partial t}\boldsymbol{D} + \boldsymbol{J}, \tag{2.2}$$

$$\nabla \cdot \boldsymbol{D} = \rho, \tag{2.3}$$

$$\nabla \cdot \boldsymbol{B} = 0, \tag{2.4}$$

where $\boldsymbol{E}$ is the electric field strength, $\boldsymbol{D}$ is the electric displacement, $\boldsymbol{H}$ is the magnetic field strength, $\boldsymbol{B}$ is the magnetic flux density, $\boldsymbol{J}$ is the electric current density, and ρ is the electric charge density. The constitutive relations for the electromagnetic field are

$$\boldsymbol{D} = \varepsilon \boldsymbol{E} \,, \tag{2.5}$$

$$\boldsymbol{B} = \mu \boldsymbol{H} \,, \tag{2.6}$$

$$\boldsymbol{J} = \sigma \boldsymbol{E} \,, \tag{2.7}$$

where ε is the permittivity, μ is the permeability and σ is the conductivity.

To understand the wave properties of the electromagnetic field, we take the curl of Eqs. 2.1 and 2.2 and utilize the constitutive relations Eqs. 2.5, 2.6 and 2.7; thus, we have

$$\nabla \times \nabla \times \boldsymbol{E} = \mu \frac{\partial}{\partial t}\left(\nabla \times \boldsymbol{H}\right) = -\mu \frac{\partial \boldsymbol{J}}{\partial t} - \mu\varepsilon \frac{\partial^2 \boldsymbol{E}}{\partial t^2}, \tag{2.8}$$

$$\nabla \times \nabla \times \boldsymbol{H} = \nabla \times \boldsymbol{J} + \varepsilon \frac{\partial}{\partial t}\left(\nabla \times \boldsymbol{E}\right) = \nabla \times \boldsymbol{J} - \mu\varepsilon \frac{\partial^2 \boldsymbol{H}}{\partial t^2} \,. \tag{2.9}$$

Eqs. 2.8 and 2.9 can be further written as

$$\nabla \times \nabla \times \boldsymbol{E} + \mu\varepsilon \frac{\partial^2 \boldsymbol{E}}{\partial t^2} = -\mu \frac{\partial \boldsymbol{J}}{\partial t}, \tag{2.10}$$

$$\nabla \times \nabla \times \boldsymbol{H} + \mu\varepsilon \frac{\partial^2 \boldsymbol{H}}{\partial t^2} = \nabla \times \boldsymbol{J} \,. \tag{2.11}$$

Using the vector identities $\nabla \times \nabla \times \boldsymbol{A} = \nabla\left(\nabla \cdot \boldsymbol{A}\right) - \nabla^2 \boldsymbol{A}$ and $\nabla \cdot \boldsymbol{E} = \rho / \varepsilon$, Eqs. 2.10 and 2.11 become

$$\nabla^2 \boldsymbol{E} - \mu\varepsilon \frac{\partial^2 \boldsymbol{E}}{\partial t^2} = \mu \frac{\partial \boldsymbol{J}}{\partial t} + \nabla\left(\frac{\rho}{\varepsilon}\right), \tag{2.12}$$

$$\nabla^2 \boldsymbol{H} - \mu\varepsilon \frac{\partial^2 \boldsymbol{H}}{\partial t^2} = -\nabla \times \boldsymbol{J} \,. \tag{2.13}$$

For a time-harmonic sourceless region, $\partial/\partial t$ is replaced by $i\omega$, where ω

represents the circular frequency. Eqs. 2.12 and 2.13 can be further expressed as

$$\nabla^2 \boldsymbol{E} + \omega^2 \mu\varepsilon \boldsymbol{E} = 0, \tag{2.14}$$

$$\nabla^2 \boldsymbol{H} + \omega^2 \mu\varepsilon \boldsymbol{H} = 0. \tag{2.15}$$

Eqs. 2.14 and 2.15 are vector wave equations for a time-harmonic field. To solve these equations analytically, vectorial wave functions are employed in the corresponding coordinate systems. In the next section, we will further utilize these two equations to express the CV beams.

2.2 Mathematical foundation of CV beams

Eqs. 2.14 and 2.15 indicate the vectorial properties of an electromagnetic field. Because visible light represents a specific type of electromagnetic field, optical phenomena obey these rules. CV beams that possess inhomogeneous polarization states have been generated in the past few decades and have attracted a substantial amount of attention. To fully establish the mathematical foundations for solving these CV beam problems, it is first convenient to consider the scalar wave equations [35]. We then rewrite Eq. 2.14 in the scalar Helmholtz equation form as

$$(\nabla^2 + k^2)E = 0, \tag{2.16}$$

where $k = \omega(\mu\varepsilon)^{1/2} = \omega/c$ is the wave number in vacuum for the field and c is the speed of light. The solution to this equation represents Hermite-Gaussian

beams in rectangular coordinates (x, y, z) and Laguerre-Gaussian beams in cylindrical coordinates (r, ϕ, z) [5]. When the CV beams propagate in the z direction, the solution can be written in the following form:

$$E(r,\phi,z,t) = g(r,\phi,z)\exp[i(kz-\omega t)]. \tag{2.17}$$

Substituting Eq. 2.17 into Eq. 2.16 and referring to the identity $\nabla^2 A = \frac{1}{r}\frac{\partial}{\partial r}\left(r\frac{\partial A}{\partial r}\right)+\frac{1}{r^2}\frac{\partial^2 A}{\partial \phi^2}+\frac{\partial^2 A}{\partial z^2}$, we subsequently have the following differential equation

$$\frac{1}{r}\frac{\partial}{\partial r}\left(r\frac{\partial g}{\partial r}\right)+\frac{1}{r^2}\frac{\partial^2 g}{\partial \phi^2}+\frac{\partial^2 g}{\partial z^2}+2ik\frac{\partial g}{\partial z}=0. \tag{2.18}$$

In practical applications, we usually take into account the slowly varying and paraxial approximations for the CV beam: $\partial^2 g/\partial z^2 \approx 0$. Therefore, $g(r, \phi, z)$ is the solution of the following scalar wave equation:

$$\frac{1}{r}\frac{\partial}{\partial r}\left(r\frac{\partial g}{\partial r}\right)+\frac{1}{r^2}\frac{\partial^2 g}{\partial \phi^2}+2ik\frac{\partial g}{\partial z}=0. \tag{2.19}$$

For this differential equation, a solution in an elementary Gaussian form can be found and can be written as [35]

$$g\left(r,z\right) = \frac{w_0}{w(z)}\exp[-i\Phi(z)]\exp(-\frac{r^2/w_0^{\,2}}{1+iz/R}) \quad . \tag{2.20}$$

Here, $g(r, z)$ is independent of the azimuthal angle. In this expression, $w(z)=w_0[1+(z/R)^2]^{1/2}$, where w_0 is the beam waist, $R = kw_0^2/2$ is the Rayleigh

range, and $\Phi(z) = \tan^{-1}(z/R)$ represents the Gouy phase shift. As noted by Hall [35], other solutions also satisfy Eq. 2.19 and can be observed as the higher-order form. When we substitute Eq. 2.20 into Eq. 2.17, the electric field $E(r, \phi, z, t)$ is obtained.

The scalar Helmholtz equations above can well describe the properties of spatially homogenous polarized light, such as linearly and circularly polarized beams, along its propagation direction. However, once we focus on spatially inhomogeneous polarized light, the scalar Helmholtz equations are no longer suitable. To accurately describe the propagation properties of the CV beam, the vector Helmholtz equation should be employed. Eq. 2.10 can then be rewritten as

$$\nabla \times \nabla \times \mathbf{E} - k^2 \mathbf{E} = 0 . \tag{2.21}$$

The solution to Eq. 2.21 can be expressed in a similar form as Eq. 2.17, but with vectorial information, as follows

$$\mathbf{E}(r, \phi, z, t) = \mathbf{G}(r, \phi, z) \exp[i(kz - \omega t)] , \tag{2.22}$$

where the amplitude [5, 35-37]

$$\mathbf{G}\left(r, \phi, z\right) = G_r\left(r, \phi, z\right)\boldsymbol{e}_r + G_\phi\left(r, \phi, z\right)\boldsymbol{e}_\phi \tag{2.23}$$

is a transverse vector component and $\boldsymbol{e}_r$ and $\boldsymbol{e}_\phi$ are unit vectors in the $\boldsymbol{r}$ and $\boldsymbol{\phi}$ directions, respectively. It should be noted that the component in the $\boldsymbol{z}$ direction is very small and can be neglected in practice; therefore, we only

need to take the $\boldsymbol{e}_r$ and $\boldsymbol{e}_\phi$ components into account in most cases. Here, G_r and G_ϕ are functions of z. In many fundamental works, it was proven that the expressions for G_r and G_ϕ contain the elementary Gaussian mode part, as shown in Eq. 2.20. In fact, when the form of $\mathbf{E}(r, \phi, z, t)$ is defined, the solutions will be fixed accordingly.

Recently, a general solution for the CV beams was obtained by Chun-Fang Li [38, 39] using the angular spectrum method, in which every component of the electric field is written in a spectrum form after the vector Helmholtz Eq. 2.21 is introduced. Next, by making use of the orthogonal properties of the vectors, $\mathbf{E}(r, \phi, z, t)$ is finally expressed as an integration. The final results of this expression show that there are other solutions (e.g., modified Bessel-Gaussian solutions) for the vector Helmholtz Eq. 2.21. Here, for simplicity, we mainly follow the traditional procedures to solve the vector equation and discuss the frequently applied cases, which have been verified by experiments.

Taking the curl of Eq. 2.22, we obtain

$$\begin{aligned}\nabla \times \boldsymbol{E} &= \nabla \times \left[\left(G_r \boldsymbol{e}_r + G_\phi \boldsymbol{e}_\phi \right) e^{i(kz-\omega t)} \right] \\ &= \boldsymbol{e}_r \left[-\left(\frac{\partial G_\phi}{\partial z} + ikG_\phi \right) \right] e^{i(kz-\omega t)} \\ &\quad + \boldsymbol{e}_\phi \left[\frac{\partial G_r}{\partial z} + ikG_r \right] e^{i(kz-\omega t)} \\ &\quad + \boldsymbol{e}_z \left[\frac{1}{r} \frac{\partial \left(rG_\phi \right)}{\partial r} - \frac{1}{r} \frac{\partial G_r}{\partial \phi} \right] e^{i(kz-\omega t)}\end{aligned} . \tag{2.24}$$

After this step, there is an $\boldsymbol{e}_z$ component. Then, by taking the curl of Eq. 2.24

again, we have

$$
\begin{aligned}
&\nabla\times\nabla\times\boldsymbol{E}\\
&=\nabla\times\left\{\left\{\boldsymbol{e}_r\left[-\left(\frac{\partial G_\phi}{\partial z}+ikG_\phi\right)\right]+\boldsymbol{e}_\phi\left[\frac{\partial G_r}{\partial z}+ikG_r\right]\right.\right.\\
&\quad\left.\left.+\boldsymbol{e}_z\left[\frac{1}{r}\frac{\partial\left(rG_\phi\right)}{\partial r}-\frac{1}{r}\frac{\partial G_r}{\partial\phi}\right]\right\}e^{i(kz-\omega t)}\right\}\\
&=\left\{\boldsymbol{e}_r\left\{\frac{1}{r}\frac{\partial}{\partial\phi}\left\{\frac{1}{r}\left[\frac{\partial\left(rG_\phi\right)}{\partial r}-\frac{\partial G_r}{\partial\phi}\right]\right\}-\frac{\partial}{\partial z}\left[\frac{\partial G_r}{\partial z}+ikG_r\right]-ik\left[\frac{\partial G_r}{\partial z}+ikG_r\right]\right\}\right.\\
&\quad+\boldsymbol{e}_\phi\left\{-\frac{\partial}{\partial z}\left[\frac{\partial G_\phi}{\partial z}+ikG_\phi\right]-ik\left[\frac{\partial G_\phi}{\partial z}+ikG_\phi\right]-\frac{\partial}{\partial r}\left\{\frac{1}{r}\left[\frac{\partial\left(rG_\phi\right)}{\partial r}-\frac{\partial G_r}{\partial\phi}\right]\right\}\right\}\\
&\quad\left.+\boldsymbol{e}_z\left\{\frac{1}{r}\frac{\partial}{\partial r}\left[r\left(\frac{\partial G_r}{\partial z}+ikG_r\right)\right]+\frac{1}{r}\frac{\partial}{\partial\phi}\left[\frac{\partial G_\phi}{\partial z}+ikG_\phi\right]\right\}\right\}e^{i(kz-\omega t)}\\
&=\left\{\boldsymbol{e}_r\left\{\frac{1}{r}\frac{\partial}{\partial\phi}\left\{\frac{1}{r}\left[\frac{\partial\left(rG_\phi\right)}{\partial r}-\frac{\partial G_r}{\partial\phi}\right]\right\}-\frac{\partial^2 G_r}{\partial z^2}-2ik\frac{\partial G_r}{\partial z}+k^2G_r\right\}\right.\\
&\quad+\boldsymbol{e}_\phi\left\{-\frac{\partial^2 G_\phi}{\partial z^2}-2ik\frac{\partial G_\phi}{\partial z}+k^2G_\phi-\frac{\partial}{\partial r}\left\{\frac{1}{r}\left[\frac{\partial\left(rG_\phi\right)}{\partial r}-\frac{\partial G_r}{\partial\phi}\right]\right\}\right\}\\
&\quad\left.+\boldsymbol{e}_z\left\{\frac{1}{r}\left[\left(\frac{\partial G_r}{\partial z}+ikG_r\right)+r\left(\frac{\partial^2 G_r}{\partial r\partial z}+ik\frac{\partial G_r}{\partial r}\right)+\left(\frac{\partial^2 G_\phi}{\partial\phi\partial z}+ik\frac{\partial G_\phi}{\partial\phi}\right)\right]\right\}\right\}\\
&\quad\times e^{i(kz-\omega t)}
\end{aligned}
\qquad \text{. (2.25)}
$$

Substituting Eqs. 2.22 and 2.25 into Eq. 2.21, we obtain the following coupled equations for the $\boldsymbol{r}$, $\boldsymbol{\phi}$ and $\boldsymbol{z}$ directions. During this procedure, the slowly varying approximations and paraxial conditions ($\partial^2 G_{r,\phi}/\partial z^2 \approx 0$, $\partial G_{r,\phi}/\partial z << kG_{r,\phi}$) are considered, and we have

$$
\frac{1}{r}\frac{\partial}{\partial\phi}\left\{\frac{1}{r}\left[\frac{\partial\left(rG_\phi\right)}{\partial r}-\frac{\partial G_r}{\partial\phi}\right]\right\}-2ik\frac{\partial G_r}{\partial z}=0\,, \qquad (2.26)
$$

$$\frac{\partial}{\partial r}\left\{\frac{1}{r}\left[\frac{\partial\left(rG_\phi\right)}{\partial r}-\frac{\partial G_r}{\partial \phi}\right]\right\}+2ik\frac{\partial G_\phi}{\partial z}=0\,, \tag{2.27}$$

$$G_r+r\frac{\partial G_r}{\partial r}+\frac{\partial G_\phi}{\partial \phi}=0\,. \tag{2.28}$$

These equations are finally simplified by substituting Eq. 2.28 into Eqs. 2.26 and 2.27 as follows:

$$\frac{1}{r}\frac{\partial}{\partial r}\left(r\frac{\partial G_r}{\partial r}\right)+\frac{1}{r^2}\frac{\partial^2 G_r}{\partial \phi^2}-\frac{1}{r^2}G_r-\frac{2}{r^2}\frac{\partial G_\phi}{\partial \phi}+2ik\frac{\partial G_r}{\partial z}=0\,, \tag{2.29}$$

$$\frac{1}{r}\frac{\partial}{\partial r}\left(r\frac{\partial G_\phi}{\partial r}\right)+\frac{1}{r^2}\frac{\partial^2 G_\phi}{\partial \phi^2}-\frac{1}{r^2}G_\phi-\frac{2}{r^2}\frac{\partial G_r}{\partial \phi}+2ik\frac{\partial G_\phi}{\partial z}=0\,. \tag{2.30}$$

These two equations are coupled differential equations for the G_r and G_ϕ components.

A convenient method to solve the above equations is to choose an appropriate solution form and substitute it into the equation. Here, the vector $\boldsymbol{G}(r, \phi, z)$ in cylindrical coordinates can be expressed as [12, 37, 40]

$$\mathbf{G}(r,\phi,z)=Q(r,z)\left\{\cos\left[(n-1)\phi+\phi_0\right]\boldsymbol{e}_r+\sin\left[(n-1)\phi+\phi_0\right]\boldsymbol{e}_\phi\right\}. \tag{2.31}$$

The expression used here is a general form for CV beams. In [35], Hall demonstrated the general form of the solutions. By using Eq. 2.31, the calculation becomes simpler compared with Hall's work because the relation between the $\boldsymbol{e}_r$ component and the $\boldsymbol{e}_\phi$ component is fixed. It should be noted, some solutions are not involved during the simplification and the final results are part of the infinite set of solutions achieved by Hall.

After inserting the G_r and G_ϕ of Eq. 2.31 into Eqs. 2.29 and 2.30, we may

obtain the simplified form

$$\frac{1}{r}\frac{\partial}{\partial r}\left(r\frac{\partial Q}{\partial r}\right)-\frac{n^2}{r^2}Q+2ik\frac{\partial Q}{\partial z}=0\,, \tag{2.32}$$

which is a partial differential equation. As we have discussed above, the solutions to Eq. 2.32 should contain the elementary Gaussian part and can be expressed in a closed form as [5, 35-37]

$$Q(r,z)=\frac{w_0}{w(z)}\exp[-i\Phi(z)]\exp\left(-\frac{r^2/w_0^{\,2}}{1+iz/L}\right)\exp\left[-\frac{i\beta^2 z/(2k)}{1+iz/L}\right]J_n\left(\frac{\beta r}{1+iz/L}\right), \tag{2.33}$$

where J_n is the nth-order Bessel function of the first kind and β is a constant parameter for the beam scale. It should be noted that $\exp[-i\Phi(z)]$ is missing in [37, 40]. The electrical field for the CV beam is then

$$\begin{aligned}\mathbf{E}(r,\phi,z,t)&=\mathbf{G}(r,\phi,z)\exp[i(kz-\omega t)]\\&=Q(r,z)\left\{\cos\left[(n-1)\phi+\phi_0\right]\boldsymbol{e}_r+\sin\left[(n-1)\phi+\phi_0\right]\boldsymbol{e}_\phi\right\}\exp[i(kz-\omega t)]\end{aligned}. \tag{2.34}$$

This is a general form of the electric field for CV beams. Many interesting phenomena have emerged from this type of light. With the development of generation methodologies for CV beams, further insight into these beams will be obtained, which may significantly enrich focal optics. We can observe two special cases from Eq. 2.34; when $n = 1$ and $\phi_0 = 0$, Eq. 2.34 becomes

$$\mathbf{E}(r,\phi,z,t)=Q(r,z)\exp[i(kz-\omega t)]\boldsymbol{e}_r\,, \tag{2.35}$$

which represents radially polarized light, and when n = 1 and $\phi_0 = \pi/2$, Eq. 2.34 can be written as

$$\mathbf{E}(r,\phi,z,t) = Q(r,z)\exp[i(kz-\omega t)]\boldsymbol{e}_{\phi}, \tag{2.36}$$

whereby the CV beam is azimuthally polarized. These two types of polarized light will be further discussed in detail.

2.3 Focusing properties of CV beams

Due to the development of generation technologies, interesting phenomena of the focused CV beams have been theoretically characterized and realized in experiments. These focused beams are widely utilized due to their unique properties. Using radially polarized light as an example, a longitudinally polarized field is enhanced in a high-NA optical system. When this beam passes through the optical element, the longitudinal component of this beam is spatially separated from the transverse part due to the apodization effect, which enables control of the shape of the focus [5].

To analyze the focusing properties of CV beams, a reliable mathematical foundation is necessary. As a basic tool, this foundation should be consistent with the experiment results. To achieve this goal, we derive expressions of the electromagnetic field in the focal region and discuss the conditions where they are applicable.

2.3.1 Generalized representations for the focal field

Airy first analyzed the focusing problem of a circle lens based on the wave theory of light [41]. Since then, substantial efforts have been made in this area, and significant results have been achieved. Fourier theory, which has been shown to be a powerful and effective tool in solving electromagnetism problems, was employed in most of the previous models [42]. By transforming a spatial problem into a spectrum problem, the field in the focal region is expressed in a more accessible form, which is easy to calculate.

When applying this theory in an optical system, the electromagnetic field for the focal region can be described by a superposition of plane waves. For each plane wave, the wave vector is $\boldsymbol{k}$, and its components k_x, k_y, and k_z represent the spatial frequencies in the $\boldsymbol{x}$, $\boldsymbol{y}$ and $\boldsymbol{z}$ directions in Cartesian coordinates, respectively. The relation between $\boldsymbol{k}$, k_x, k_y and k_z is given by $k_x^2 + k_y^2 + k_z^2 = k^2$. The complex field $\boldsymbol{E}(x', y', z')$ is then expressed in the Fourier form using the following procedures [24, 42, 43] (shown in Figure 2.1)

$$\boldsymbol{E}(k_x, k_y, z') = \int\int_{-\infty}^{+\infty} \boldsymbol{E}(x', y', z') e^{-i(k_x x' + k_y y')} dx' dy' \,. \tag{2.37}$$

The field is then expressed as

$$\boldsymbol{E}(x', y', z') = \frac{1}{(2\pi)^2} \int\int_{-\infty}^{+\infty} \boldsymbol{E}(k_x, k_y, z') e^{i(k_x x' + k_y y')} dk_x dk_y \,. \tag{2.38}$$

Here, $\boldsymbol{E}(x', y', z')$ is a known quantity. For an arbitrary point M, its electric field can be expressed by utilizing Eq. 2.38 as follows:

$$\boldsymbol{E}(x,y,z)=\frac{1}{(2\pi)^2}\int\int_{-\infty}^{+\infty}\boldsymbol{E}(k_x,k_y,z')e^{i\left[k_x x+k_y y+k_z(z-z')\right]}dk_x dk_y \ . \tag{2.39}$$

The value of k_z is $(k^2-k_x^2-k_y^2)^{1/2}$ when $k_x^2+k_y^2\le k^2$ and $i(k_x^2+k_y^2-k^2)^{1/2}$ when $k_x^2+k_y^2\ge k^2$.

Eq. 2.39 presents the electric field of an arbitrary point. We may further derive the Rayleigh-I and Rayleigh-II integrals based on this formula [42, 43].

To address the focusing problems of CV beams, the geometrical theory of light is also considered, and this means that the spherical wave needs to converge to the focal point *O* to satisfy the actual situation. As Figure 2.2 shows, after passing through the reference aperture, the incident CV beams form a specific distribution near the point *O*. When we calculate the electric field, it is hard to directly obtain the results based on Eq. 2.39. Usually, a semi-analytical plane-wave expansion method is utilized.

We suppose that the field in the aperture *D* is given by [24, 42]

$$E(x',y',z')=E_M(x',y')\frac{e^{-ikR}}{R}, \tag{2.40}$$

where *R* is the distance from a general point *M* to the focal point *O*. Here, the point *M* is in the aperture. The function $E_M(x',y')$ is an amplitude and phase function for the incident spherical wave. The electric field in the aperture can then be expressed as follows in the angular spectrum form by making use of Eq. 2.37:

$$E(k_x,k_y,z')=\iint_D E_M(x',y')\frac{e^{-ikR}}{R}e^{-i\left(k_x x'+k_y y'\right)}dx'dy' \ . \tag{2.41}$$

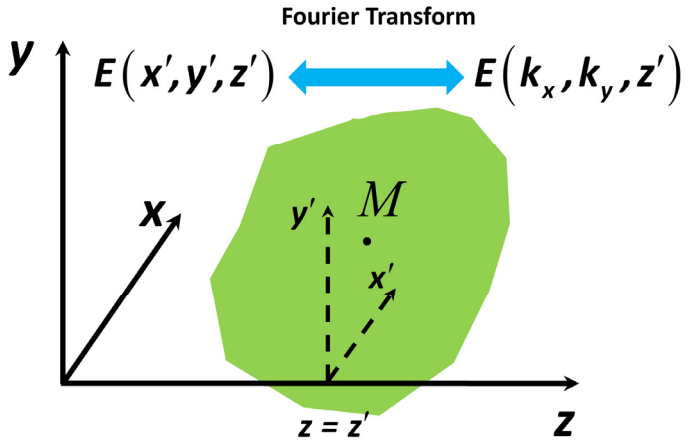

Figure 2.1. The electrical field $\boldsymbol{E}(x', y', z')$ and its Fourier form $\boldsymbol{E}$ (k_x, k_y, z') are given in the reference plane $z = z'$.

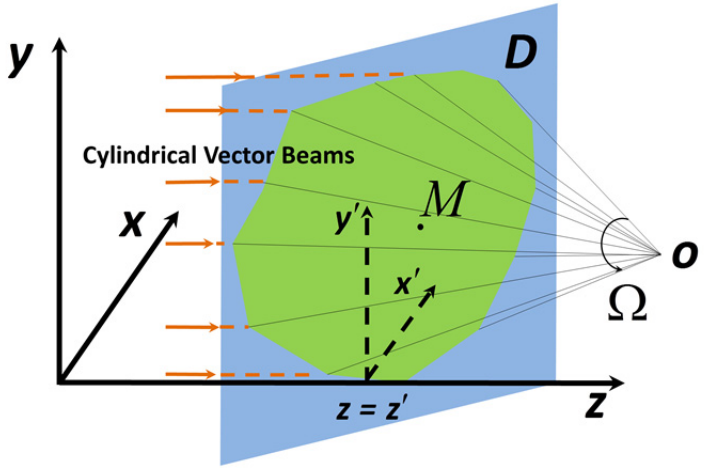

Figure 2.2. The schematic of focusing a CV beam. M is an arbitrary point in the aperture. All incident waves converge to the focus O after passing through the aperture.

Eq. 2.41 can be further approximated in the following form, which was obtained by Debye in 1909 [44],

$$E(k_x, k_y, z') = \frac{2\pi}{ik_z} E_M\left(x_o - \frac{k_x}{k_z}(z_o - z'), y_o - \frac{k_y}{k_z}(z_o - z')\right) \times e^{-i\left[k_x x_o + k_y y_o + k_z (z_o - z')\right]}, \quad (2.42)$$

where (x_o, y_o, z_o) is the position of the focal point O. According to the laws of geometrical optics, after passing the aperture, the incident CV beam forms a

light cone and a solid angle Ω, as shown in Figure 2.2.

Substituting Eq. 2.42 into Eq. 2.39, we obtain

$$E(x,y,z) = -\frac{i}{2\pi}\iint_{\Omega} E_M\left(x_o - \frac{k_x}{k_z}(z_o - z'), y_o - \frac{k_y}{k_z}(z_o - z')\right) \times \frac{e^{i\left[k_x(x-x_o)+k_y(y-y_o)+k_z(z-z_o)\right]}}{k_z} dk_x dk_y \quad . \tag{2.43}$$

Eq. 2.43 is called the Debye integral [45]. This integral is an accurate approximation of the electromagnetic field in the focal region under the condition $k(z_o - z') >> \pi/\sin^2(\theta/2)$, where θ represents the half-focusing geometry aperture angle [45]. It can be further expressed in a vector form. In most cases, we have chosen the aperture plane as the reference plane, and z' equals zero. Then, Eq. 2.43 is expressed in the following form that was first derived by E. Wolf [24]:

$$\boldsymbol{E}(x,y,z) = -\frac{i}{2\pi}\iint_{\Omega} \frac{\boldsymbol{a}\left(k_x, k_y\right)}{k_z} e^{i\boldsymbol{k}\cdot(\boldsymbol{r}-\boldsymbol{r}_o)} dk_x dk_y \,, \tag{2.44}$$

where $\boldsymbol{a}\left(k_x, k_y\right) = \boldsymbol{E}_M\left(x_o - z_o k_x / k_z, y_o - z_o k_y / k_z\right)$.

Here, the electric field for the focal region is obtained. As a fundamental criterion, this result provided a substantial tool to the field of optics and directly led to a large number of discoveries; simultaneously, it promoted the development of microscopy. When we review the derivation procedure discussed above, it is worth noting that an important step is to obtain the relation between the aperture field distributions and the focal field, as in Eq.

2.42. In addition, a compromise solution that maintains simplicity and rigor has been adopted in the derivation. This procedure is more explicit than E. Wolf's derivation and simultaneously maintains mathematical accuracy.

2.3.2 Calculations for the focused CV beams

When we analyze the focusing properties of the CV beams, the extended Richards-Wolf's vector diffraction method developed by K. S. Youngworth and T. G. Brown is frequently used [5, 46]. The schematic structure for focusing the beam is shown in Figure 2.3. For a given CV beam, we assume a plane wavefront to illuminate the objective lens, and the incident field can be written in another form of Eq. 2.34 as [5]

$$\boldsymbol{E}_{inc} = l_0 Q(r)\left\{\cos\left[(n-1)\phi_0 + \varphi\right]\boldsymbol{e}_0 + \sin\left[(n-1)\phi_0 + \varphi\right]\boldsymbol{e}_1\right\}, \quad (2.45)$$

where l_0 is the amplitude of the incident CV light on the pupil plane and $Q(r)$ is the normalized distribution amplitude function. The unit vectors $\boldsymbol{e}_0$ and $\boldsymbol{e}_1$ applied for the incident CV beam can be expressed by the unit vectors of the reference coordinate shown in Figure 2.3 as

$$\boldsymbol{e}_0 = \cos\phi_1 \boldsymbol{e}_x + \sin\phi_1 \boldsymbol{e}_y, \quad (2.46)$$

$$\boldsymbol{e}_1 = \boldsymbol{e}_0 \times \boldsymbol{k}. \quad (2.47)$$

Here, $\boldsymbol{k}$ is the unit vector along the $\boldsymbol{z}$ direction, and the incident CV beam propagates in that direction. After passing the objective lens, the distribution

on the incident surface is transformed into a spherical wavefront by the projection function $p(\theta)$

$$\frac{r}{f} = p(\theta), \tag{2.48}$$

where f is the focal length, as shown in Figure 2.3.

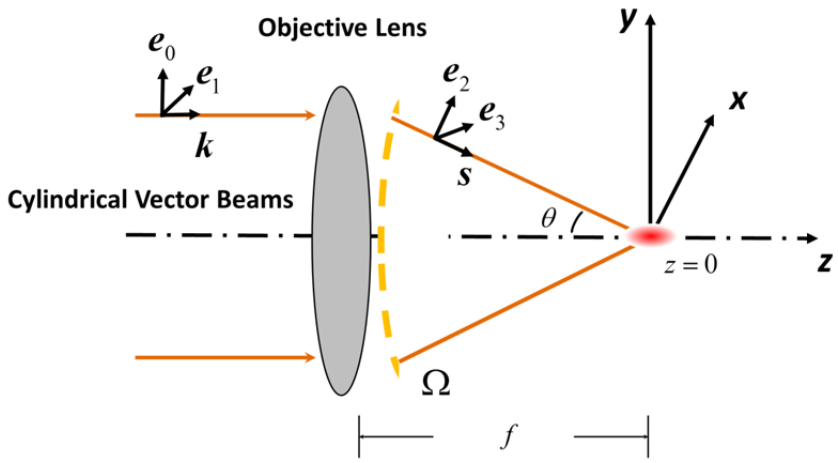

Figure 2.3. A schematic for the focusing of a CV beam. $\boldsymbol{e}_0$, $\boldsymbol{e}_1$ and $\boldsymbol{k}$ are unit vectors of the incident CV beam, and $\boldsymbol{e}_2$, $\boldsymbol{e}_3$ and $\boldsymbol{s}$ are unit vectors for the focused CV beam.

Based on the actual situation, all the light becomes concentrated in the focal region. Therefore, the spherical wavefront apodization function $Q(\theta)$ may be obtained under the requirement of energy conservation, as shown in Figure 2.4, and the relation is expressed as

$$\begin{aligned}&[l_0 Q(r)]^2 \pi\left[(r+dr)^2 - r^2\right] \\ &\quad = [l_0 Q(\theta)]^2 2\pi f\left\{\left[f - f\cos(\theta + d\theta)\right] - \left[f - f\cos\theta\right]\right\}\end{aligned}, \tag{2.49}$$

where $\pi[(r+dr)^2 - r^2]$ is the annulus area for the incident wavefront plane, and the corresponding spherical area is $2\pi f\{[f - f\cos(\theta + d\theta)] - [f - f\cos\theta]\}$.

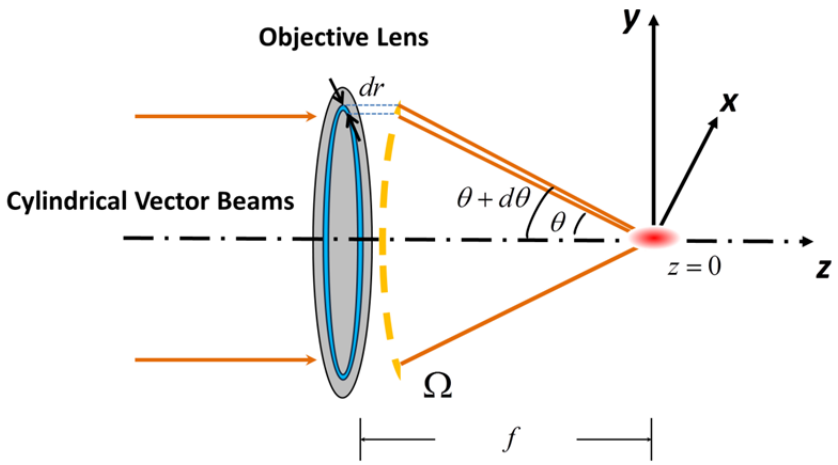

Figure 2.4. The incident CV beam is converted into a spherical wave after passing through the objective lens. The apodization function can be achieved under the requirement of energy conservation. Here, *dr* is the differential of the annulus area, while *dθ* is the differential of the corresponding spherical area.

Expanding Eq. 2.49, the high-order part is extremely small and can thus be neglected. Finally, it is simplified as

$$[l_0 Q(r)]^2 2\pi r dr = [l_0 Q(\theta)]^2 2\pi f^2 \sin\theta d\theta , \tag{2.50}$$

and we then have [5]

$$Q(\theta) = Q(r)\sqrt{\frac{p(\theta)p'(\theta)}{\sin\theta}} = Q(fp(\theta))\sqrt{\frac{p(\theta)p'(\theta)}{\sin\theta}} . \tag{2.51}$$

For a typical sine condition at the objective lens, the ray projection function is $r/f = \sin\theta$, that is, $p(\theta) = \sin\theta$, and this is utilized in Richards-Wolf's most cited study [25]. The apodization function is then simplified as

$$Q(\theta) = Q(f\sin\theta)\sqrt{\cos\theta} . \tag{2.52}$$

From Figure 2.4, we can also write out the relations between the unit vectors

of the focused beam and the reference unit vectors as

$$\boldsymbol{e}_2 = \cos\theta(\cos\phi_1\boldsymbol{e}_x + \sin\phi_1\boldsymbol{e}_y) + \sin\theta\boldsymbol{e}_z\,, \tag{2.53}$$

$$\boldsymbol{e}_3 = \boldsymbol{e}_1 = -\sin\phi_1\boldsymbol{e}_x + \cos\phi_1\boldsymbol{e}_y\,. \tag{2.54}$$

Using these relations, the electric field for the focal region can be obtained. In the former section, we have obtained a general expression for the imaging plane. Applying Wolf's formula (Eq. 2.44), and subsequently, we obtain

$$\boldsymbol{E} = \frac{-ik}{2\pi}\iint_{\Omega}\boldsymbol{a}(\theta,\phi_1)e^{ik(\boldsymbol{s}\cdot\boldsymbol{r})}d\Omega\,, \tag{2.55}$$

where $kd\Omega=dk_xdk_y/k_z$. When the aperture is limited to a circular focusing geometry, as shown in Figure 2.3, the field is found to be

$$\boldsymbol{E} = \frac{-ik}{2\pi}\int_0^{\theta_{\max}}d\theta\int_0^{2\pi}\boldsymbol{a}(\theta,\phi_1)e^{ik(\boldsymbol{s}\cdot\boldsymbol{r})}\sin\theta d\phi_1\,, \tag{2.56}$$

where $\theta_{\max}$ is the maximal focusing angle of the objective lens, and the field strength factor $\boldsymbol{a}(\theta,\phi_1)$ for the focusing CV beam is [5, 46]

$$\boldsymbol{a}(\theta,\phi_1) = l_0 fQ(\theta)[\cos\left[(n-1)\phi_0+\varphi\right]\boldsymbol{e}_2 + \sin\left[(n-1)\phi_0+\varphi\right]\boldsymbol{e}_3]\,. \tag{2.57}$$

In addition, we use the vectors derived above to express the phase in the integration

$$\boldsymbol{s}\cdot\boldsymbol{r} = z\cos\theta + r\sin\theta\cos(\phi_1-\phi)\,. \tag{2.58}$$

Substituting Eqs. 2.57 and 2.58 into Eq. 2.56, the electric field in the focal region becomes

$$
\begin{aligned}
\boldsymbol{E} &= \frac{-ik}{2\pi}\int_0^{\theta_{\max}} d\theta \int_0^{2\pi} l_0 f Q(\theta)\left(\cos\left[(n-1)\phi_1+\varphi\right]\boldsymbol{e}_2+\sin\left[(n-1)\phi_1+\varphi\right]\boldsymbol{e}_3\right) \\
&\quad \times e^{ik(z\cos\theta+r\sin\theta\cos(\phi_1-\phi))}\sin\theta d\phi_1 \\
&= \frac{-iA}{\pi}\int_0^{\theta_{\max}} d\theta \int_0^{2\pi} Q(\theta)\left(\cos\left[(n-1)\phi_1+\varphi\right]\boldsymbol{e}_2+\sin\left[(n-1)\phi_1+\varphi\right]\boldsymbol{e}_3\right) \\
&\quad \times e^{ik(z\cos\theta+r\sin\theta\cos(\phi_1-\phi))}\sin\theta d\phi_1 \\
&= \frac{-iA}{\pi}\int_0^{\theta_{\max}} d\theta \int_0^{2\pi} Q(\theta)\left[\cos\left[(n-1)\phi_1+\varphi\right]\begin{pmatrix}\cos\theta\cos\phi_1\boldsymbol{e}_x\\ \cos\theta\sin\phi_1\boldsymbol{e}_y\\ \sin\theta\boldsymbol{e}_z\end{pmatrix}\right. \\
&\quad \left.+\sin\left[(n-1)\phi_0+\varphi\right]\begin{pmatrix}-\sin\phi_1\boldsymbol{e}_x\\ \cos\phi_1\boldsymbol{e}_y\\ 0\boldsymbol{e}_z\end{pmatrix}\right] e^{ik(z\cos\theta+r\sin\theta\cos(\phi_1-\phi))}\sin\theta d\phi_1 \\
&= \frac{-iA}{\pi}\int_0^{\theta_{\max}} d\theta \int_0^{2\pi} Q(\theta) \\
&\quad \times\begin{pmatrix}\left\{\cos\left[(n-1)\phi_1+\varphi\right]\cos\theta\cos\phi_1-\sin\left[(n-1)\phi_1+\varphi\right]\sin\phi_1\right\}\boldsymbol{e}_x\\ \left\{\cos\left[(n-1)\phi_1+\varphi\right]\cos\theta\sin\phi_1+\sin\left[(n-1)\phi_1+\varphi\right]\cos\phi_1\right\}\boldsymbol{e}_y\\ \cos\left[(n-1)\phi_1+\varphi\right]\sin\theta\boldsymbol{e}_z\end{pmatrix} \\
&\quad \times e^{ik(z\cos\theta+r\sin\theta\cos(\phi_1-\phi))}\sin\theta d\phi_1
\end{aligned}
\qquad ,(2.59)
$$

where the constant A is given by $A=\pi f l_0/\lambda$. We write Eq. 2.59 in cylindrical coordinates for convenience in further calculations and refer to the following identities:

$$\boldsymbol{e}_r = \cos\phi\boldsymbol{e}_x + \sin\phi\boldsymbol{e}_y, \tag{2.60}$$

$$\boldsymbol{e}_\phi = -\sin\phi\boldsymbol{e}_x + \cos\phi\boldsymbol{e}_y. \tag{2.61}$$

Thus, the electric field near the focal plane is

$$\boldsymbol{E} = \frac{-iA}{\pi}\int_0^{\theta_{\max}} d\theta \int_0^{2\pi} Q(\theta) \times \begin{pmatrix} \left\{\cos\left[(n-1)\phi_1+\varphi\right]\cos\theta\cos(\phi_1-\phi) - \sin\left[(n-1)\phi_1+\varphi\right]\sin(\phi_1-\phi)\right\}\boldsymbol{e}_r \\ \left\{\cos\left[(n-1)\phi_1+\varphi\right]\cos\theta\sin(\phi_1-\phi) + \sin\left[(n-1)\phi_1+\varphi\right]\cos(\phi_1-\phi)\right\}\boldsymbol{e}_\phi \\ \cos\left[(n-1)\phi_1+\varphi\right]\sin\theta\boldsymbol{e}_z \end{pmatrix} \times e^{ik(z\cos\theta + r\sin\theta\cos(\phi_1-\phi))}\sin\theta d\phi_1 \quad . (2.62)$$

For the $\boldsymbol{e}_r$ component, the coefficient is further simplified as

$$\begin{aligned} &\cos\left[(n-1)\phi_1+\varphi\right]\cos\theta\cos(\phi_1-\phi) - \sin\left[(n-1)\phi_1+\varphi\right]\sin(\phi_1-\phi) \\ &= \frac{1}{2}\cos\theta\left\{\cos(n\phi_1-\phi+\varphi) + \cos\left[(n-2)\phi_1+\phi+\varphi\right]\right\} \\ &\quad + \frac{1}{2}\left\{\cos(n\phi_1-\phi+\varphi) - \cos\left[(n-2)\phi_1+\phi+\varphi\right]\right\} \\ &= \frac{1}{2}\cos\theta\left\{\cos\left[n(\phi_1-\phi)\right]\cos\left[(n-1)\phi+\varphi\right]\right. \\ &\quad - \sin\left[n(\phi_1-\phi)\right]\sin\left[(n-1)\phi+\varphi\right] \\ &\quad + \cos\left[(n-2)(\phi_1-\phi)\right]\cos\left[(n-1)\phi+\varphi\right] \\ &\quad \left. - \sin\left[(n-2)(\phi_1-\phi)\right]\sin\left[(n-1)\phi+\varphi\right]\right\} \\ &\quad + \frac{1}{2}\left\{\cos\left[n(\phi_1-\phi)\right]\cos\left[(n-1)\phi+\varphi\right]\right. \\ &\quad - \sin\left[n(\phi_1-\phi)\right]\sin\left[(n-1)\phi+\varphi\right] \\ &\quad - \cos\left[(n-2)(\phi_1-\phi)\right]\cos\left[(n-1)\phi+\varphi\right] \\ &\quad \left. + \sin\left[(n-2)(\phi_1-\phi)\right]\sin\left[(n-1)\phi+\varphi\right]\right\} \end{aligned} \quad . (2.63)$$

Similarly, for the $\boldsymbol{e}_\phi$ component and the $\boldsymbol{e}_z$ component, the coefficients can also be further simplified as

$$
\begin{aligned}
&\cos\left[(n-1)\phi_1+\varphi\right]\cos\theta\sin(\phi_1-\phi)\\
&\quad+\sin\left[(n-1)\phi_1+\varphi\right]\cos(\phi_1-\phi)\\
&=\frac{1}{2}\cos\theta\left\{\sin(n\phi_1-\phi+\varphi)-\sin\left[(n-2)\phi_1+\phi+\varphi\right]\right\}\\
&\quad+\frac{1}{2}\left\{\sin(n\phi_1-\phi+\varphi)+\sin\left[(n-2)\phi_1+\phi+\varphi\right]\right\}\\
&=\frac{1}{2}\cos\theta\left\{\sin\left[n(\phi_1-\phi)\right]\cos\left[(n-1)\phi+\varphi\right]\right.\\
&\quad+\cos\left[n(\phi_1-\phi)\right]\sin\left[(n-1)\phi+\varphi\right]\\
&\quad-\sin\left[(n-2)(\phi_1-\phi)\right]\cos\left[(n-1)\phi+\varphi\right]\\
&\quad\left.-\cos\left[(n-2)(\phi_1-\phi)\right]\sin\left[(n-1)\phi+\varphi\right]\right\}\\
&\quad+\frac{1}{2}\left\{\sin\left[n(\phi_1-\phi)\right]\cos\left[(n-1)\phi+\varphi\right]\right.\\
&\quad+\cos\left[n(\phi_1-\phi)\right]\sin\left[(n-1)\phi+\varphi\right]\\
&\quad+\sin\left[(n-2)(\phi_1-\phi)\right]\cos\left[(n-1)\phi+\varphi\right]\\
&\quad\left.+\cos\left[(n-2)(\phi_1-\phi)\right]\sin\left[(n-1)\phi+\varphi\right]\right\}
\end{aligned}
\quad . \tag{2.64}
$$

$$
\begin{aligned}
&\cos\left[(n-1)\phi_1+\varphi\right]\\
&=\cos\left[(n-1)(\phi_1-\phi)\right]\cos\left[(n-1)\phi+\varphi\right]\\
&\quad-\sin\left[(n-1)(\phi_1-\phi)\right]\sin\left[(n-1)\phi+\varphi\right]
\end{aligned}
\quad . \tag{2.65}
$$

Because all the components are explicitly expressed, we substitute Eqs. 2.63, 2.64 and 2.65 into Eq. 2.52. Meanwhile, we utilize the following identities:

$$\int_0^{2\pi}\cos(n\phi_1)e^{ikr\sin\theta\cos\phi_1}d\phi_1=2\pi i^n J_n(kr\sin\theta)\,, \tag{2.66}$$

$$\int_0^{2\pi}\sin(n\phi_1)e^{ikr\sin\theta\cos\phi_1}d\phi_1=0\,. \tag{2.67}$$

Finally, we obtain the electric field [5, 25, 37,46]

$$
\begin{aligned}
\boldsymbol{E}=&-i^{n+1}A\int_0^{\theta_{\max}}Q(\theta)\\
&\times\begin{pmatrix}
\cos\left[(n-1)\phi+\varphi\right]\left[\cos\theta\left(J_n-J_{n-2}\right)+\left(J_n+J_{n-2}\right)\right]\boldsymbol{e}_r\\
\sin\left[(n-1)\phi+\varphi\right]\left[\cos\theta\left(J_n+J_{n-2}\right)+\left(J_n-J_{n-2}\right)\right]\boldsymbol{e}_\phi\\
-2i\cos\left[(n-1)\phi+\varphi\right]\sin\theta J_{n-1}\boldsymbol{e}_z
\end{pmatrix}.\\
&\times e^{ikz\cos\theta}\sin\theta d\theta
\end{aligned}
\tag{2.68}
$$

Here, we obtain the electric field in the focal region for the focused CV beams in cylindrical coordinates. The derivation improved the reported studies and generalized the Richards-Wolf's vector diffraction method to arbitrary high-order situations. Because the general CV beam is chosen to be the incident illumination wave, this formula can be used to describe the focusing properties of different CV beams by setting the values of n. In the next chapter, based on this result, we will mainly focus on the situation of radially polarized light.

2.4 Summary

In this chapter, the foundations for the study of the CV beam are investigated in depth. During this procedure, a mathematical model of the focal field, which is in good agreement with the experimental results, is introduced when addressing the vector Helmholtz equations. Subsequently, a generalized expression of the CV beams is obtained. We have noticed that the radially polarized light and azimuthally polarized light are two special cases in the solution sets.

The second task in this chapter is to build the field model in the focal region. We apply Fourier theory and transform the spatial problem into a frequency spectrum problem. Through the derivation, the Debye integral for the focal field is obtained to significantly simplify the problem, and it is further interpreted in E. Wolf's form. Because the circular aperture is applied

in this thesis, we further simplify the focal problem by utilizing Richards-Wolf's vector diffraction theory, and finally, a generalized expression for the CV beam is given.

Chapter 3

Abnormal distributions in the focal field and anti-resolution

3.1 Introduction

As an important concept in diffraction theory, the point spread function (PSF) dictates the performance of an optical imaging system [23]. For a given PSF of a system, if the input pattern in the object space is $O(\xi, \eta)$, where ξ and η denote the coordinates of the object plane, the output pattern $I(x, y)$ in the image space can be expressed using the weighted integration of the object plane

$$I(x,y) = \iint_{\text{object plane}} O(\xi,\eta)\,\text{PSF}(x-\xi, y-\eta)\,d\xi\,d\eta, \qquad (3.1)$$

where $\text{PSF}(x-\xi, y-\eta)$ is the response of the system.

The theory behind the PSF was first proposed by Airy, and he gave the expression for a circular aperture based on the wave theory of light in 1835

[41]. Since then, many analyses have contributed to this area, and a large number of important results have been obtained. As examples, Rayleigh investigated the PSF for incoherent sources in 1879 [47, 48], Lommel further developed Airy's theory using two functions in 1885 and 1886 [49], and Strehl analyzed the effect of third-order aberrations and introduced an important concept known as the *Strehl definition* to evaluate the quality of a system [50].

Among these studies, a breakthrough concerning PSFs in diffraction theory is the application of a series of new circular polynomials developed by Zernike and Nijboer. In Nijboer's pioneering study [51], the case of an aberration, which is much smaller than the wavelength, was solved using a simple yet accurate solution. In addition, their methodology also provided a useful tool for evaluating the permitted aberration in an optical system.

Today, high-NA imaging systems have been widely applied in science, technology and industry. In high-NA cases, the information of the focal field is detailed, and electromagnetic field components for the focal region should not be treated as independent components as those in low-NA systems. In addition, some properties of light in high-NA systems, such as polarization and amplitude, are different from those in low-NA systems. To build an accurate model for these high-NA systems, the vectorial properties of the light should be carefully considered. After Ignatowsky and Hopkins's original and meaningful attempts in this area of study [52, 53], Richards and Wolf developed a rigorous vector diffraction methodology for studying the high-NA

situation, which has been widely used in optical system design and evaluation [24, 25]. In addition, this method has become part of the foundation of optical systems.

In modern applications, such as high-density data storage, super-resolution imaging systems, and nano particle trapping and manipulation, the diffraction theory of the PSF agrees very well with the experiments. Due to the increasing demand for insights into phenomena at the microscopic scale and for investigations into the interactions between light and materials, a super-resolution system is therefore needed. We can see from Eq. 3.1 that the imaging density distribution is uniquely determined by the system's PSF. Here, the distribution curve of the PSF stands for the system imaging ability, and subsequently, an arbitrary resolution and field distribution may be ideally achieved by the specially manipulated PSF, as shown in Figure 3.1. The PSF of a conventional imaging system, whose imaging resolution is usually limited by the diffraction limit ~λ/2NA, is represented in Figure 3.1b. To overcome the diffraction limit, many strategies, such as superlenses and hyperlenses, have been proposed to achieve super-resolution and utilized to narrow the PSF, as shown in Figure 3.1c [18, 19, 54-61]. Correspondingly, the concept of fuzzy resolution, which is generated by broadening the PSF and maintaining a constant value within the focal region, is also familiar to us in real applications (shown in Figure 3.1a). As the system response, fuzzy resolution is usually utilized in a radar system. For example, widening the PSF

in an interference system is equivalent to increasing the signal level at the radar's working frequencies. Through this method, the information is encrypted, and the radar system cannot effectively obtain an accurate position of the object.

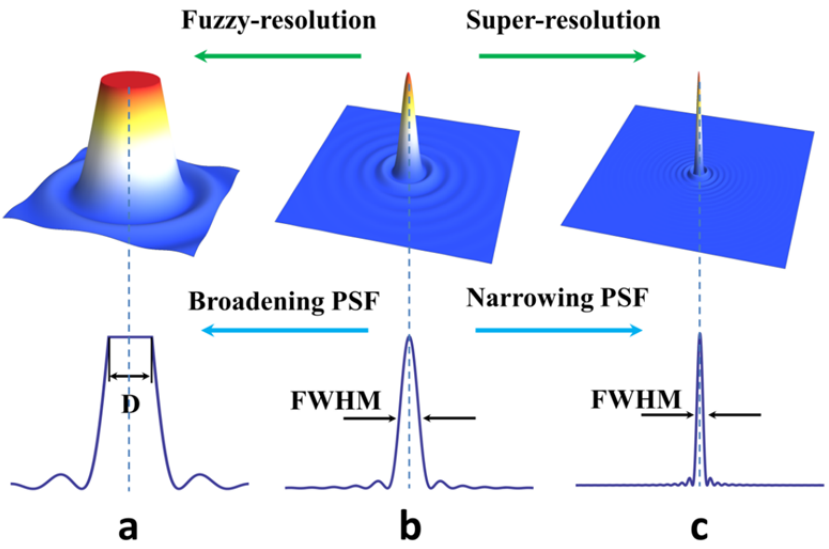

Figure 3.1. Different PSFs for imaging systems: (a) fuzzy-resolution for an optical system is generally achieved by broadening the PSF of the conventional imaging system. (b) PSF of a conventional imaging system that has a diffraction limit ~λ/2NA. (c) Super-resolution for an optical system that is obtained by narrowing the conventional PSF.

In addition to widening or narrowing the PSF to achieve the desired resolution, another interesting topic is the abnormal field distribution in the focal region. In contrast to super-resolution and fuzzy resolution, abnormal distributions mainly concern the density distribution along the beam-propagation direction. Due to the existence of the specific polarized electric field on the axis, some unexpected results have been obtained. For example, by utilizing the DOE with amplitude and phase modulation for

specific polarized CV beams, various phenomena, such as optical chains, have been realized [15].

Among these abnormal distributions, non-diffraction longitudinally polarized light has attracted a significant amount of attention for its potential applications. To generate this non-diffraction light, the phase profile of a radially polarized beam is manipulated through binary optics or phase discontinuity technology so as to broaden the PSF in the propagation direction. A beam with a uniform distribution is then obtained in the vicinity of the focus.

3.2 Focusing properties of a radially polarized Bessel-Gaussian beam

3.2.1 Focusing a radially polarized Bessel-Gaussian beam

Many experiments and numerical calculations have shown that when focusing a radially polarized CV beam in a high-NA optical system, a strong longitudinal electric component appears near the focal region. A large number of interesting applications, such as particle trapping and manipulation, second-harmonic generation, Raman spectroscopy, and high-resolution confocal fluorescence microscopy, may take advantage of this result.

To comprehensively determine the properties of a focused CV beam (shown in Figure 2.3), we can follow Richards-Wolf's vector diffraction theory and further investigate the mathematical model established in Chapter 2

using a specific case. To simplify our discussion, we limit the situation to a typical radially polarized Bessel–Gaussian beam in the following sections, and a schematic is shown in Figure 2.3. The corresponding electric fields in the focal region can be expressed as [46]

$$E_r = A\int_0^{\alpha} \sqrt{\cos\theta}\sin 2\theta l(\theta) J_1(kr\sin\theta) e^{ikz\cos\theta} d\theta , \tag{3.2}$$

$$E_z = 2iA\int_0^{\alpha} \sqrt{\cos\theta}\sin^2\theta l(\theta) J_0(kr\sin\theta) e^{ikz\cos\theta} d\theta , \tag{3.3}$$

where

$$l(\theta) = \exp\left[-\beta^2\left(\frac{\sin\theta}{\sin\alpha}\right)^2\right] J_1\left(2\beta\frac{\sin\theta}{\sin\alpha}\right). \tag{3.4}$$

Here, α=arcsin (NA), NA denotes the numerical apertures of the lenses, J_n (x) (n=0 or 1) is the n-th order Bessel function, β is the ratio of the pupil radius and the beam waist, A is a constant related to the focal length and the wavelength, and l (θ) =1 and f represent uniform illumination and focal length, respectively. Here, we chose a focusing lens with an NA equal to 0.95.

Generally speaking, Richards-Wolf's diffraction theory, in which the vertical properties of light are considered, is usually employed in a high-NA system (NA>0.6); however, it can also be used to represent the focal field in a low-NA system [40].

To describe the intensity distributions in the vicinity of the focus, Eqs. 3.2 and 3.3 will be calculated using proper methods. In most situations, these calculations are based on numerical integration and are performed by taking

samples in the relative integration interval; thus, this procedure requires considerable computation time. Some elements, such as binary optical elements, are applied in optical systems to achieve the desired distributions, and subsequently, the time for optimizing the element parameters will heavily depend on the calculation time for these two integrations. Therefore, calculations of Eqs. 3.2 and 3.3 are extremely important tasks. Recently, a much faster method was developed by extending the Zernike-Nijboer theory, and the electromagnetic field for the focal region can be expressed by a series instead of by integrations [62-68]. Compared with traditional methods, the extended Zernike-Nijboer method exhibits incredible speed and has the prospect of being applied in integrated optical systems. Taking all of this into consideration, Eqs. 3.2, 3.3 and 3.4 are still calculated through numerical integrations, and we mainly focus on the focal region due to the slowly varying and paraxial approximation conditions.

The electric field distribution on the *xy* plane is shown in Figure 3.2. As observed in Figure 3.2a, the field of the focused CV beam is mainly concentrated in the $r \leq \lambda$ region, and there is almost no energy distribution beyond this region. The highest intensity region appears on the optical axis. Along with the increase in the radius, the intensity will gradually decrease until it is equal to the background intensity level. Figure 3.2b shows the field distribution on the $z = 0.5\lambda$ plane. When propagating to this plane, the focused beam has a significant divergence. The field amplitude on the axis is equal to

73% of that in the $z = 0$ case.

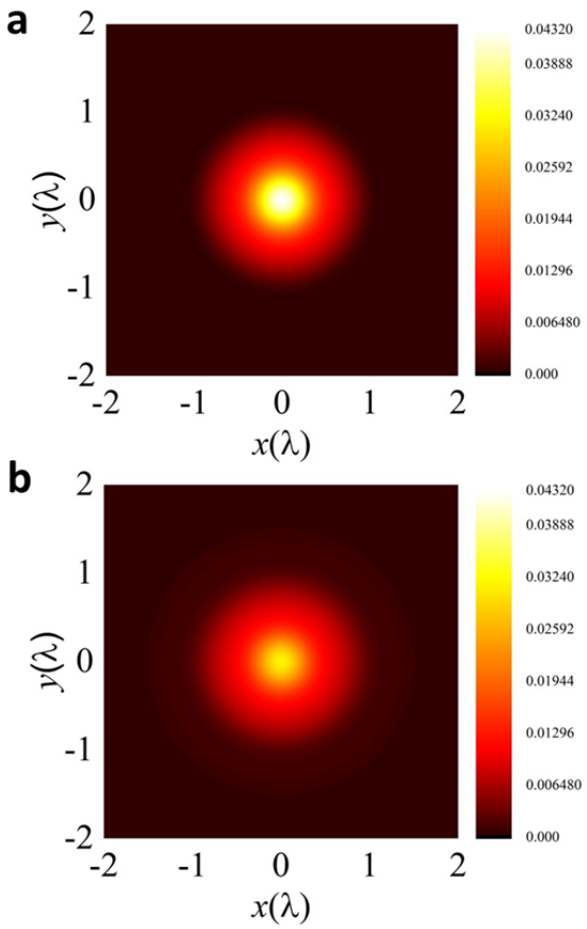

Figure 3.2. Electric-field distribution on the *xy* plane for a radially polarized Bessel-Gaussian beam. $|E|^2$ is calculated and used to represent the total electric field. (a) Field distribution on the $z = 0$ plane. (b) Field distribution on the $z = 0.5\lambda$ plane.

The electric field distribution along the beam propagation direction is shown in Figure 3.3. It can be observed that the intensity is high at a distance of λ from the focus ($z = 0$). Beyond this distance, the intensity sharply decreases and is equal to half of the maximum when $z = 0.727\lambda$. Figures 3.2 and 3.3 imply that the field intensity for a focused radially polarized CV beam only exists in a small area and that little energy can spread beyond the distance

of one wavelength. In most applications, the working region is set within this effective distance.

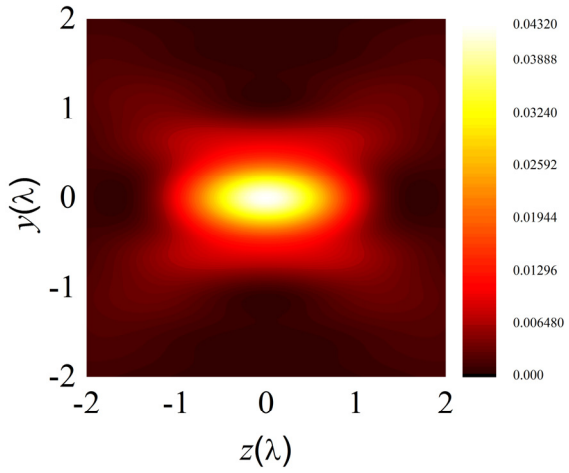

Figure 3.3. Electric-field distribution on the *yz* plane. The reference plane is arbitrarily selected and includes the optical axis.

Figure 3.4 shows the electric field distribution of different components on the $z = 0$ plane. One can observe from the figure that when $r = 0$, $|E_z|^2 = |E|^2$, which means that only the longitudinal component $|E_z|$ exists on the axis. This relation can be directly found from Eqs. 3.2 and 3.3. When r increases, the longitudinal component $|E_z|$ decreases, while the transverse component $|E_r|$ obviously increases. In a certain region ($0.32\lambda < r < 0.79\lambda$), the transverse component $|E_r|$ is the main part of the total intensity. This phenomenon implies that the longitudinal and transverse components dominate different parts of the focal region. This is because of the different apodization effects that these two components experience in a high-NA system. Therefore, they are spatially separated from each other. Interestingly, this result prompts meaningful

applications. For example, by enhancing the apodization effect and by eliminating one of the two components, a beam of high purity can be obtained.

In [69], the integral $\Gamma = 2\pi\int_0^{r_0} \left|E_{r,z}\left(z=0\right)\right|^2 rdr$ was employed to denote the electric field energy of the corresponding component in a certain region ($0 < r < r_0$) on the $z = 0$ plane. It does not contain the azimuthal part in the presentation because it is removed as a common factor. In fact, the integral is written in the origin form as

$$\Gamma = \int_0^{2\pi}\int_0^{r_0} \left|E_{r,z}(r,z)\right|^2 rdrd\phi \,. \tag{3.5}$$

In the calculations, we determine that the first zero position for the radial electric density is $r_0 = 1.055\lambda$ instead of 1.07λ [69]. By calculating Eq. 3.5, we obtain the longitudinal energy and the transverse energy in a certain region, and subsequently, the field proportions of the total field are obtained.

Figure 3.5 shows the energy proportions of the electric field in the beam propagation direction. From the result, we find that the longitudinal energy is always lower than the transverse energy in the focal region, although it exhibits a higher intensity near the axis, as shown in Figure 3.4. The maximum proportion of longitudinal energy occurs at the $z = 0$ plane. However, only 45% of the total energy is from the longitudinal part. As the beam propagates, this proportion continues decreasing. When the focused beam propagates to the $z = \lambda$ plane, the transverse component generates more than 60% of the total energy. The variation in this energy proportion reflects the strict governing of

Maxwell's equations in the focal region. When the position leaves the focal plane (z = 0), the longitudinal component E_z starts to fade, as indicated in Figure 3.5. Meanwhile, the transverse component E_r, which plays an important role in enabling the light to propagate, starts to emerge.

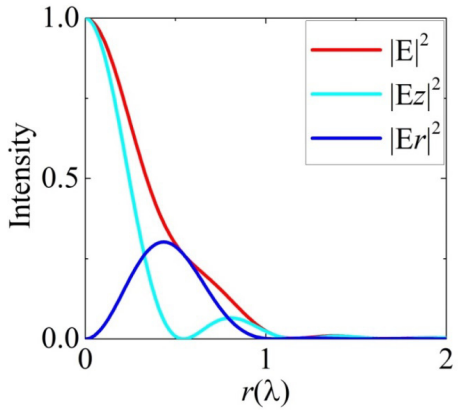

Figure 3.4. Electric-field distributions of different components on the xy plane (z = 0). $|E_z|^2$ represents the longitudinally polarized field intensity, and $|E_r|^2$ represents the radially polarized field intensity.

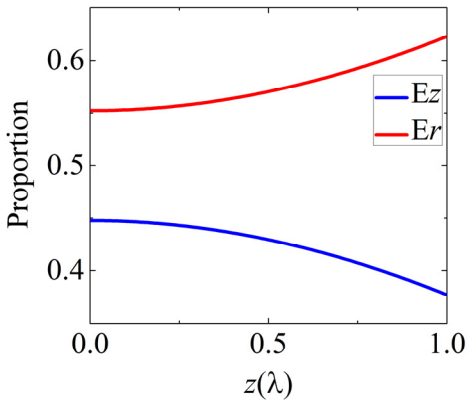

Figure 3.5. Electric field energy proportions in the propagation direction. $|E_z|$ represents the longitudinal energy proportion in the total field, and $|E_r|$ represents the radially polarized field proportion in the total field.

3.2.2 Generation of non-diffraction light

For a focused radially polarized CV beam, it has been shown that the energy mainly concentrates in a region one wavelength away from the focus. When passing through this area, the light rapidly diverges due to diffraction. Although most applications benefit from this focusing property, it limits the development of some important techniques. Therefore, one of the main objectives in focusing optics for a long time was to obtain a focus with a deeper depth. Ideally, it is desirable to have a non-diffraction polarized beam with a uniform intensity distribution along the propagation direction. This mysterious phenomenon was first theoretically predicted by Durnin in 1987 [70, 71]. Since then, it has attracted a significant amount of attention for its potential applications [72-87].

It is known that the zeroth-order Bessel beam is diffraction free when it propagates in free space [70]. This beam has a field form of $J_0(k_1 r)\exp(ik_2 z)$, where $k_1^2 + k_2^2 = k^2$, k is the wave number, and J_0 is the zeroth-order Bessel function. When $0 < k_1 < k$, $J_0(k_1 r)\exp(ik_2 z)$ represents a non-diffraction beam. Experimentally, beams with finite power, such as Bessel-Gaussian beams and Laguerre-Gaussian beams, are employed to realize the near non-diffraction phenomenon.

From the discussions in the previous section, we acknowledge that the working distance for a focused, radially polarized beam is far from meeting the diffraction-free requirement. To achieve a non-diffracting beam with a

longer depth of focus (DOF), one of the most frequently used methods is to add an additional diffraction optical element to the optical system. Based on the type of this element, it functions in a manner similar to a special phase or amplitude modulator, which polarizes the beam longitudinally while maintaining the intensity uniformly distributed within a certain distance.

As observed in Figure 3.6, a BOE referred to in Chapter 1, which simply generates a phase change in the CV beam, is employed to realize the diffraction-free beam. A Bessel-Gaussian beam propagates through the BOE and the focusing lens from left to right.

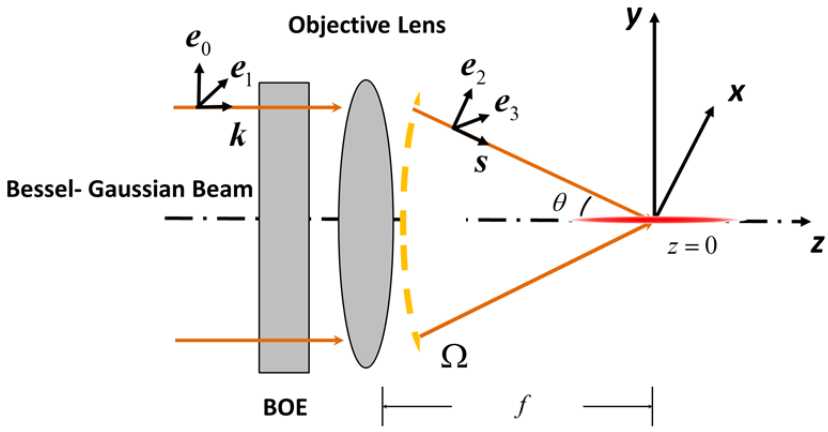

Figure 3.6. Schematic to realize a non-diffraction beam. A BOE is added to the optical system.

Figure 3.7 presents the electric field distribution on the *xy* plane when adding a BOE to the system. As observed in Figure 3.7a, the radius for the full-width at half maximum (FWHM) area is 0.432λ, which is equal to 63.5% of that in the case without the BOE, and the highest intensity area also appears on the optical axis. Some energies exhibit a non-continuous distribution in the

observing area; however, they are rather small when compared with those in the highest region. Figure 3.7b shows the field distribution on the z=0.5λ plane. When propagating to this plane, the focused CV beam has the same distribution as in Figure 3.7a. The intensity amplitude on the axis is equal to 99.7% of that when z = 0. When we select additional planes along the axis and investigate the field distributions, it is found that the field distributions at different planes have similar profiles as that in Figure 3.7, which implies that the focused CV beam can propagate without diffraction.

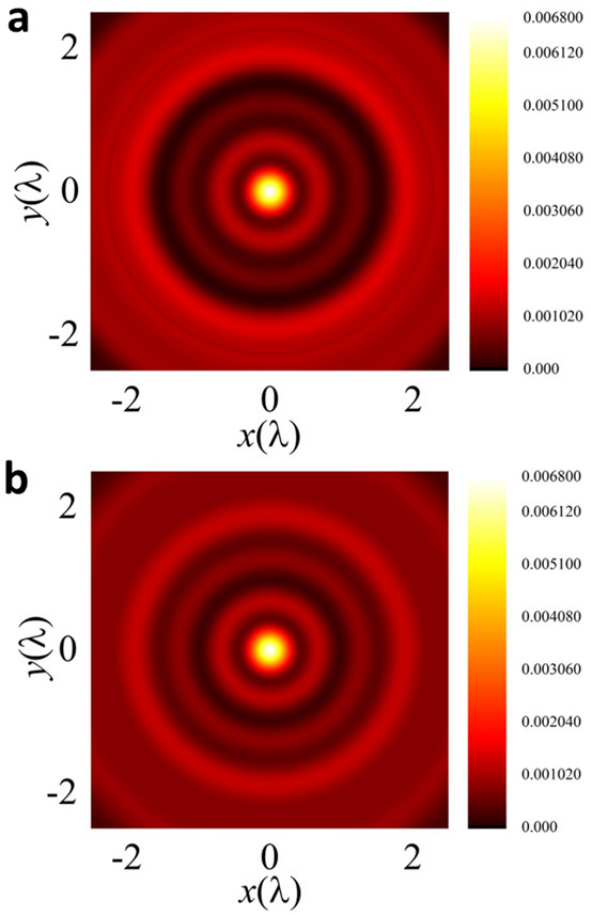

Figure 3.7. Electric-field distributions on the xy plane for a radially polarized Bessel-Gaussian beam when a BOE is applied to the system. (a) Field distribution on the z = 0 plane. (b) Field distribution on the z = 0.5λ plane.

When we observe the situation in the beam propagation direction, one impressive result is that the DOF is significantly extended. As observed from Figure 3.8, the intensity is uniformly distributed for a distance of 4λ, which is much longer than that previously achieved. Nevertheless, beyond the non-diffractive distance, the light diverges as well. Recently, a much longer DOF has been achieved using an electric dipole array optimization model, and the length for the uniform distribution was as long as 8λ [17].

To show the changes in the electric components when a BOE is added to the system, we could further draw the field distributions of different components on the $z = 0$ plane. It is observed in Figure 3.9 that when $r = 0$, $|E_z|^2 = |E|^2$. Compared with the initial results, we find that only a longitudinal polarized field could exist on the axis regardless of a BOE being applied to the system. When $0 < r < 0.336\,\lambda$, the longitudinal component $|E_z|$ becomes the main part of the total field. In this region, $|E_z|$ rapidly decreases, whereas the transverse $|E_r|$ component slowly increases. It should be noted that the FWHM is reduced to 0.432λ, which, consequently, means that a higher resolution is achieved.

Figures 3.10 and 3.11 show the field distributions of the longitudinal and radial components on five selected planes in the beam propagation direction, respectively. E_z dominates within the area close to the beam axis ($r < 0.3\lambda$), and it has almost the same profile in the diffraction-free region ($r < 2\lambda$). When the beam propagates to the $r = 2\lambda$ plane, a small but clear divergence is observed.

Figure 3.11 shows that E_r is almost smeared out within the central region around the beam axis. When it deviates more from the central axis, E_r gradually increases. It has a similar distribution in the propagation direction as well.

From Figure 3.10 and 3.11, it is evident that in the non-diffraction distance, the value of $|E_z|/|E_r|$ is nearly constant in a certain region close to the beam axis, and this indicates a fixed proportion of the total energy.

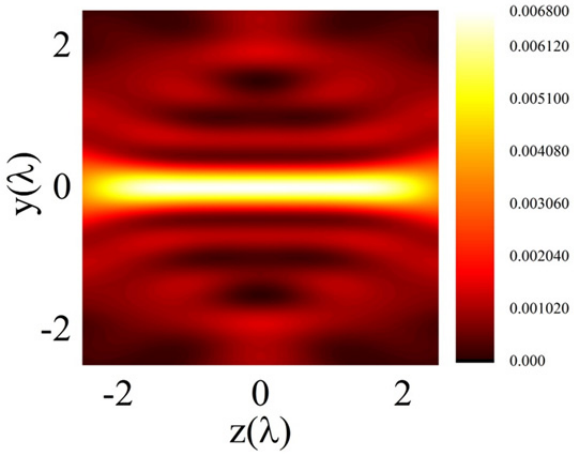

Figure 3.8. Electric-field distributions on the *yz* plane for a radially polarized Bessel-Gaussian beam when a BOE is added to the system.

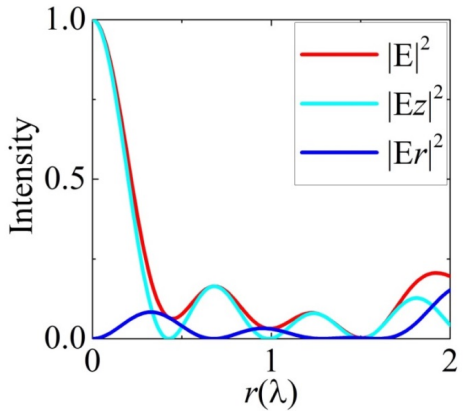

Figure 3.9. Electric-field distributions of different components on the *xy* plane (z = 0) for a radially polarized Bessel-Gaussian beam when a BOE is added to the system.

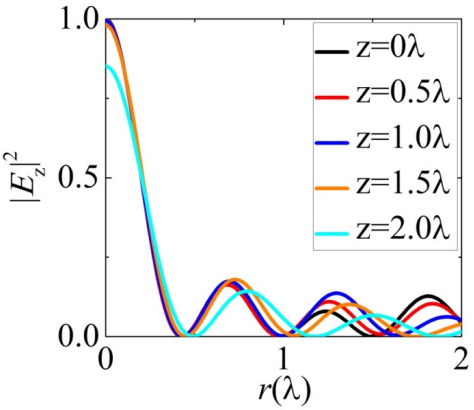

Figure 3.10. Longitudinal polarized field intensity on the transversal cut planes when a BOE is added to the system.

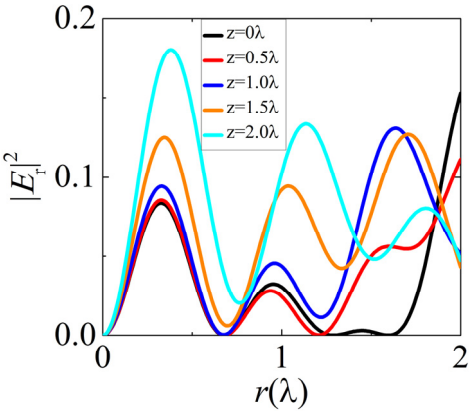

Figure 3.11. Radial polarized field intensity on the transversal cut planes when a BOE is added to the system.

To verify our predictions above, we draw Figure 3.12 to show the energy proportions of the electric field in the beam propagation direction. It is found that the energy from the longitudinal component is always higher than that from the transverse component in the non-diffraction region ($0 < z < 2\lambda$), which is completely different from that in the case without the BOE. At the same time, the maximum proportion for $|E_z|$ appears on the $z = 0$ plane, and approximately 80% of the total energy is longitudinally polarized. When

propagating to the $z = 1.5\lambda$ plane, the focused CV beam still maintains a high beam purity, and 70% of the total energy is generated by the longitudinal component. Recently, it has been confirmed that a higher purity (86% of the total energy) can be achieved using a dipole optimization model [17].

This example explicitly showed that the field distribution of the focal region will change if a BOE is added to the system. This result attracts our attention and heralds the introduction of new phenomena that have never been explored before.

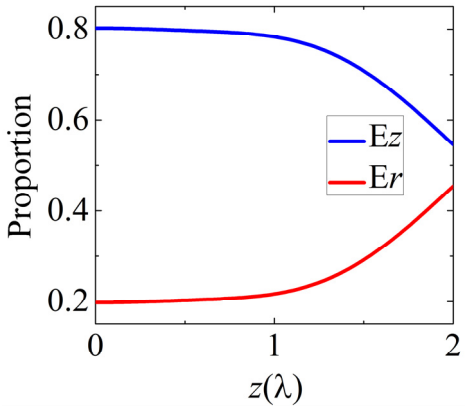

Figure 3.12 Electric field energy proportions in the propagation direction. A BOE is added to the system.

3.3 Anti-resolution

3.3.1 PSF for AR

In the past decade, numerous methods to magnify the evanescent waves and produce perfect images have been proposed and verified [18, 54-57]. However, these magnified evanescent waves quickly decay when they leave the

superlens, making it very difficult to apply in practice. Thus, the 'hyperlens' was proposed to convert evanescent fields into propagation waves, which successfully pushes the perfect imaging boundary beyond the lens [19, 58-61].

As we have discussed and shown above, the focus has thus been confined to realize super-resolution and perfect imaging through minimizing the span of the PSF in imaging systems for use in novel applications. However, no one seems to have raised the question of what new interesting phenomena and applications may exist if one pushes the limit toward the other extreme, as shown in Figure 3.13, i.e., suppressing and flattening the PSF of the optical system until it completely vanishes. This new scheme, defined as anti-resolution (AR), could create a macroscopic spatial region with a nearly perfect null-field region that light could simply bypass.

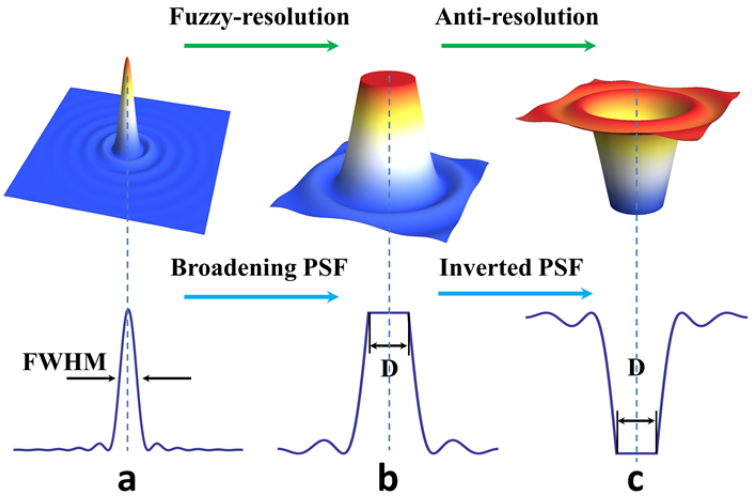

Figure 3.13. Generation of AR. D: the dimension of the flattened regime. When D becomes extremely large and when the magnitude therein is completely smeared out, AR can be achieved. (a) PSF of a conventional imaging system. (b) Fuzzy-resolution PSF. (c) AR PSF.

3.3.2 Generation of AR PSF

From the concept of AR, we know that the key tasks of realizing the AR phenomenon are to establish and investigate the right model; to study the vanished PSF, as shown in Figure 3.13c; and to characterize the performance of this phenomenon. From previous discussions, it is known that a surface-shape-based BOE can be applied to control the wavefront based on the requirements. Based on this knowledge, we apply a BOE to realize this phenomenon.

Figure 3.14 presents a feasible physical setup for AR generation, which is composed of multi-silica rings (BOE) and a focusing lens. Here, a $0-\pi$ phase mask is utilized, and the thickness of the concentric silica groove can be designed such that when the light passes through the groove, it will have an additional π-phase difference compared with the light passing through the neighboring air belts. A radially polarized CV beam is chosen as the incident beam. When passing through the diffraction phase mask, its wavefront changes, and a new wavefront is generated based on the surface shape of the BOE. The effects of the lens are focusing and bending, and all the light will concentrate on the focal region after passing through it.

This problem can be further exhibited in a mathematical model using a functional form. For example, $T(\theta) = e^{i\phi(\theta)}$ denotes the transmission function that characterizes the phase modulation mask, as shown in of Figure 3.14. A multi-belt silica groove is used as our phase modulation mask, with $\phi(\theta) = 0$ or

$\phi(\theta) = \pi$ corresponding to different ranges of the angle θ, i.e.,

$$T(\theta) = \begin{cases} 1, & \text{for } 0 < \theta < \theta_1, \theta_2 < \theta < \theta_3, \theta_4 < \theta < \alpha, \\ -1, & \text{for } \theta_1 < \theta < \theta_2, \theta_3 < \theta < \theta_4. \end{cases} \tag{3.6}$$

Here, α=arcsin (NA), and NA denotes the numerical aperture of the focusing lens. The angles θ_i (i=1, 2, 3, 4) correspond to the individual radius $r_i = \sin\theta_i$ /NA (normalized by the radius R of the lens).

It is shown in Figure 3.15 that each radius corresponds to a certain phase. When the light passes through different parts of the phase mask, a phase of −1 or 1 will be added, and a new wavefront is yielded. The additional phase is not limited to π. If the groove depth is not an integral multiple of the wavelength, a fraction phase can be obtained.

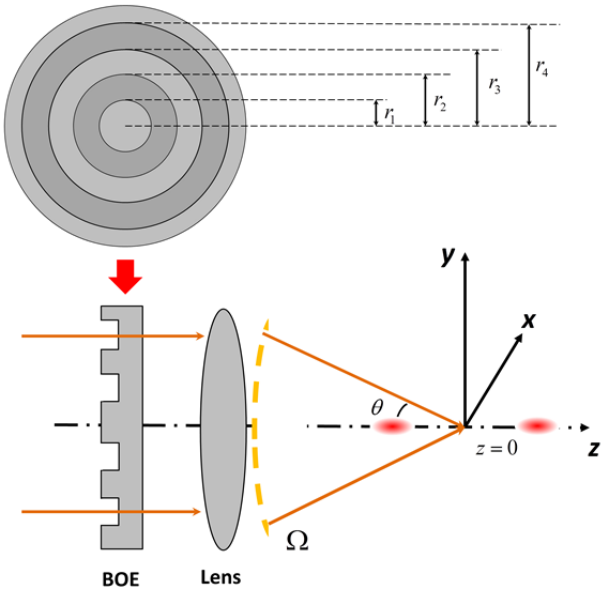

Figure 3.14 Physical configurations for realizing AR, where a Bessel-Gaussian beam propagates through the specially designed silica mask and focusing lens from left to right.

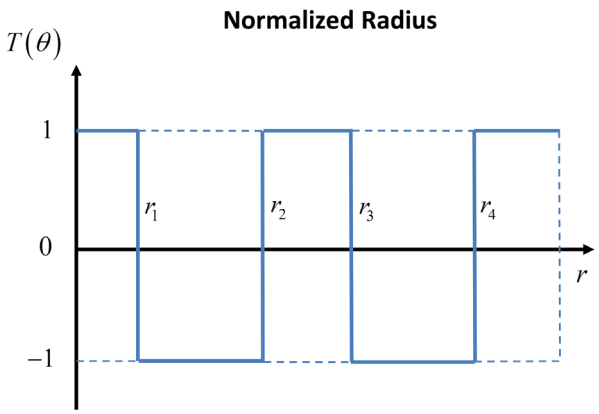

Figure 3.15 Field transmission functions for the mask. Here, the diffractive mask is treated as a pure phase element and changes the wavefront of only the incident radially polarized CV beam.

When the radially polarized Bessel-Gaussian beam passes through this BOE and the focusing lens, the transmission function Eq. 3.6 should be added to Eqs. 3.2 and 3.3. The electric field in the focal region is expressed as

$$E_r = A\int_0^{\alpha} \sqrt{\cos\theta}\,\sin 2\theta l(\theta) T(\theta) J_1(kr\sin\theta) e^{ikz\cos\theta} d\theta\,, \tag{3.7}$$

$$E_z = 2iA\int_0^{\alpha} \sqrt{\cos\theta}\,\sin^2\theta l(\theta) T(\theta) J_0(kr\sin\theta) e^{ikz\cos\theta} d\theta\,. \tag{3.8}$$

By calculating these two quantities, we can obtain the field distribution at the focal region. To achieve the AR phenomenon (i.e., a flat, smeared-out PSF, as shown in Figure 3.13c), a three-dimensional electromagnetic null-field region (as shown in Figure 3.16) with the size of a few wavelengths in the transversal direction and in the longitudinal direction is needed.

When we study the AR field distributions, $|E_r|^2 + |E_z|^2 = 0$ must be satisfied in that region. By substituting all variables into Eqs. 3.7 and 3.8, the question can be transformed into a solution-finding problem. Unfortunately,

no closed-form expressions can be obtained using known mathematical methods.

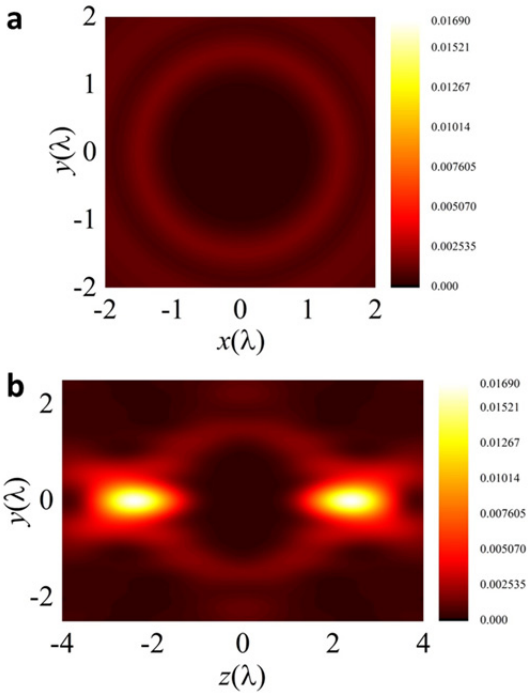

Figure 3.16 Electric-field distributions on the *xy* plane ($z = 0$) and *yz* plane for a radially polarized Bessel-Gaussian beam when a diffractive phase mask is added in the system. (a) Field distribution on the *xy* plane ($z = 0$). (b) Field distribution on the *yz* plane.

To find suitable solutions, we return to the starting point and re-examine the physical model of the scheme. It is evident that the physical structure of the setup for this system is symmetric, which must lead to a field with a symmetric distribution. Furthermore, if the electric-field distribution is required to be zero, the distributions in the central region should fulfill this requirement first. This conclusion provides critical information regarding the electromagnetic null field. Because this is a continuous physical problem, if the electric-field distribution on the axis is forced to be zero, the intensity in

the region near the axis must also approach zero.

Based on the analysis above, we can successfully transform the three-dimensional problem into a one-dimensional problem, making it much simpler than before. By forcing the intensity on the optical axis to zero while requiring that the PSF must vanish within a certain range, we can obtain the parameters for the phase-mask optics element.

Because the optimization procedure is iterative, the parameters of the diffractive phase mask are not strictly defined. Here, we present some optimized results and describe the evolution of the AR phenomenon. Figures 3.17, 3.18 and 3.19 present the AR field-intensity distributions with different binary phase masks. In Figure 3.17, the normalized parameters of the BOE are $r_1 = 0$, $r_2 = 0.1163$, $r_3 = 0.2691$, $r_4 = 0.6022$, $r_5 = 0.8892$, and $r_6 = 1$. The field distribution on the beam axis indicates that the electromagnetic null field exists only on the $z = 0$ plane. In this case, the area of the null field is rather small, and the situation is similar to that of the previous studies. When we investigate the field distribution from a three-dimensional perspective, the low-intensity area is found to be surrounded by a wall-like electric field. Additionally, as we adjust the parameters of the phase mask, the intensity distribution near the focal region varies. Thus, by resetting the parameters to $r_1 = 0$, $r_2 = 0.1163$, $r_3 = 0.4469$, $r_4 = 0.7176$, $r_5 = 0.9264$, and $r_6 = 1$, we can achieve the field distribution depicted in Figure 3.18. It is evident from Figure 3.18b that the null-field area is much larger than before, and the distance between the

two focuses is enlarged from 3.7λ to nearly 4.5λ. However, there are still some non-zero regions on the intensity boundary that delimits the entire area. As the optimization progresses, many solutions that satisfy the specified requirements can be obtained. To make all of the energy move to the side wall, the parameters can be further optimized to $r_1 = 0$, $r_2 = 0.1163$, $r_3 = 0.5489$, $r_4 = 0.6022$, $r_5 = 0.7901$, and $r_6 = 1$. In Figure 3.19, it is evident that the null-intensity field is increased to nearly 5 wavelengths in the z direction, whereas the intensity is still equal to zero (as shown in Figure 3.19a). The area of this null field is as large as $4\lambda^2$. During the optimization, we find that once the area of the null field reaches this size, no further significant improvement is obtained, meaning that the region of the AR effect has a finite volume.

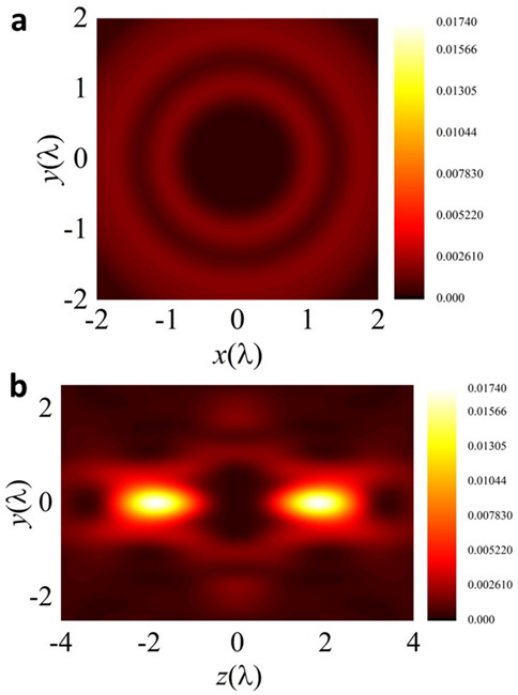

Figure 3.17. Electric-field distribution of the new optical bending scheme based on AR with a lens of NA=0.95. The parameters of the phase mask are $r_1 = 0$, $r_2 = 0.1163$, $r_3 = 0.2691$, $r_4 = 0.6022$, $r_5 = 0.8892$, and $r_6 = 1$. (a) Field distribution on the xy plane ($z = 0$). (b) Field distribution on the yz plane.

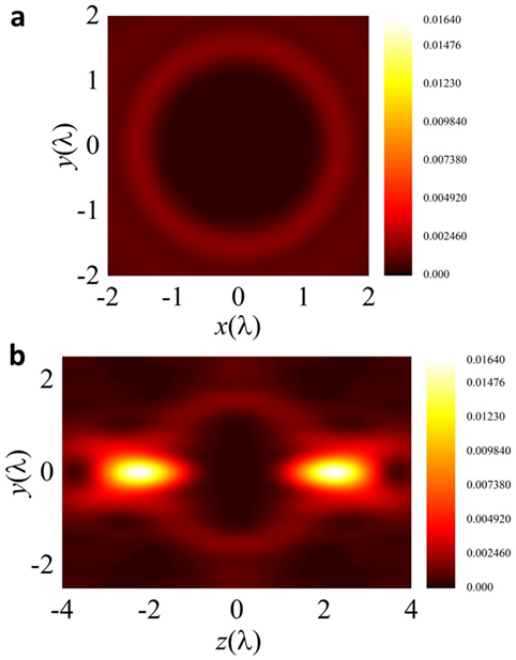

Figure 3.18. Electric-field distribution of the new optical bending scheme based on AR with a lens of NA=0.95. The parameters of the phase mask are $r_1 = 0$, $r_2 = 0.1163$, $r_3 = 0.4469$, $r_4 = 0.7176$, $r_5 = 0.9264$, and $r_6 = 1$. (a) Field distribution on the *xy* plane ($z = 0$). (b) Field distribution on the *yz* plane.

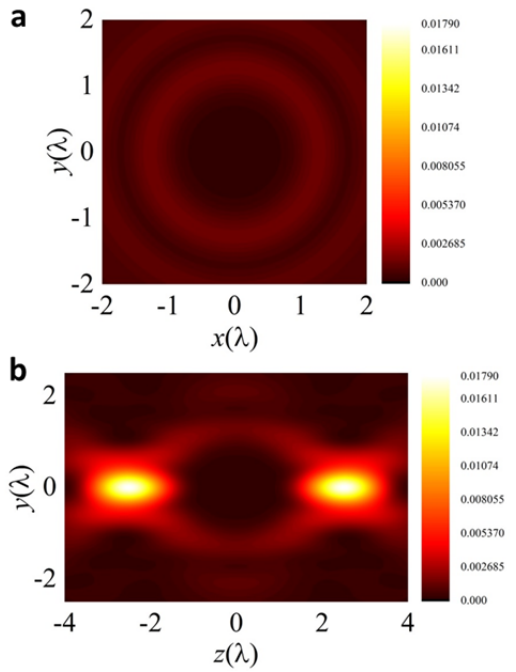

Figure 3.19. Electric-field distribution of the new optical bending scheme based on AR with a lens of NA=0.95. The parameters of the phase mask are $r_1 = 0$, $r_2 = 0.1163$, $r_3 = 0.5489$, $r_4 = 0.6022$, $r_5 = 0.7901$, and $r_6 = 1$. (a) Field distribution on the *xy* plane ($z = 0$). (b) Field distribution on the *yz* plane.

The new optical bending phenomenon is quite interesting. As is apparent from the images above, the field distribution can be separated into two parts. In addition to the null-field part, which is surrounded by a wall-like electric field, another clear feature of the intensity distribution is the high-intensity points. There are two focuses in a single system, and they have the same shape. This scheme, which bends the light trajectories without superluminal propagation [88] or metamaterials and without falling back on the classical Gouy effect [89], exhibits the features of self-imaging beams for the first time in a physical configuration.

To illustrate this interesting property of the AR configuration, we present the field distributions on seven cut planes at specified locations from the left-most focus to the right-most focus in Figure 3.20. The self-imaging property is clearly demonstrated, and the envelope of the null field (its boundary) can be visualized from the varying ring sizes. Note that the electric field on the beam axis is longitudinally polarized only. At the two focusing points, the electric field on the beam axis ($r = 0$) is purely longitudinally polarized, as can be determined from Eqs. 3.7 and 3.8.

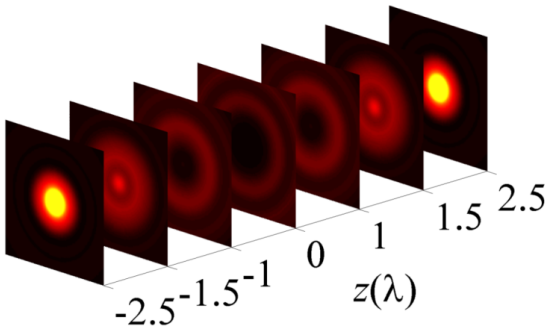

Figure 3.20. Electric-field distribution of the new optical bending scheme based on AR with a lens of NA=0.95 [Appendix B 1]. Seven cut planes at equal separation distances are depicted to demonstrate the individual transversal field intensities.

In principle, this methodology is not limited by the state of polarization; therefore, azimuthally polarized incidence is examined in Figure 3.21 using the expressions of Eqs. 3.9-3.11. A null-field region is observed with approximately the same size as before, indicating that the AR effect is insensitive to the polarization. Similar results can also be achieved for other polarization states, such as linear polarization and circular polarization.

$$E_{\phi} = 2A\int_{0}^{\alpha} \sqrt{\cos\theta}\sin\theta l(\theta)T(\theta)J_1(kr\sin\theta)e^{ikz\cos\theta}d\theta, \tag{3.9}$$

$$H_r = -A\int_{0}^{\alpha} \sqrt{\cos\theta}\sin(2\theta)l(\theta)T(\theta)J_1(kr\sin\theta)e^{ikz\cos\theta}d\theta, \tag{3.10}$$

$$H_z = -2iA\int_{0}^{\alpha} \sqrt{\cos\theta}\sin^2\theta l(\theta)T(\theta)J_0(kr\sin\theta)e^{ikz\cos\theta}d\theta. \tag{3.11}$$

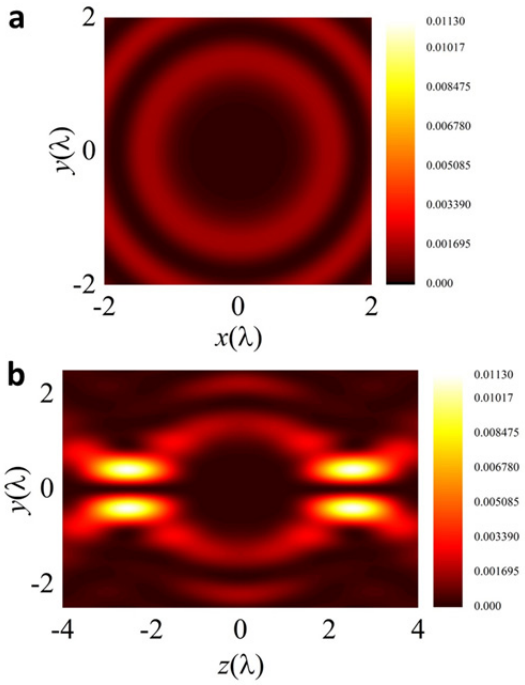

Figure 3.21. Electric-field distribution of the new optical bending scheme based on AR with a lens NA=0.95. An azimuthally polarized light is chosen as the incident wave. The parameters of the phase mask are $r_1 = 0$, $r_2 = 0.1163$, $r_3 = 0.5489$, $r_4 = 0.6022$, $r_5 = 0.7901$, and $r_6 = 1$. (a) Field distribution on the *xy* plane ($z = 0$). (b) Field distribution on the *yz* plane.

3.3.3 Design of the BOE to realize AR

In the previous section, we demonstrated the tight focusing of the vector beams (i.e., radially and azimuthally polarized beams) using a high-NA lens. In a tightly focused CV beam, the electric field in the focal region exhibits a strong dependence of the incident vector beam on the polarization, e.g., Eqs. 3.7 and 3.8 for a radially polarized beam and Eq. 3.9 for an azimuthally polarized beam. Therefore, it is not convenient to provide a general description of the BOE design. For simplicity, we consider a focusing lens of low NA as an example. In this case, the polarization effect in the focal region is not significant and can be neglected [Appendix B 1].

For incident beams with different polarizations, the electric field in the focal region can be described in a unified manner using a scalar focusing of the light with a low-NA lens, and the field in the focal region can be expressed as [90]

$$U(\rho,z)=\frac{i2\pi}{\lambda z}e^{ik(z+\frac{\rho^2}{2z})}\int_0^R u_0(r)\cdot e^{\frac{ikr^2}{2z}}e^{-\frac{ikr^2}{2f}}J_0\left(\frac{kr\rho}{z}\right)rdr, \tag{3.12}$$

where f is the focal length, R is the radius of the focusing lens, $u_0(r)$ is the electric field incident on the focusing lens, and $\exp(-ikr^2/f)$ is the equivalent phase factor of the low-NA lens, which is located at $z=0$. It is implied that the electric field at the focal plane can be obtained by setting $z=f$ in Eq. 3.12. From Eq. 3.12, by setting $z=f$ and omitting the constant factor $i2\pi/(\lambda f)\cdot\exp[ik(z+0.5\rho^2/f)]$, we find the following expression for the electric field at the focal plane:

$$\begin{aligned}
U(\rho)&=\int_0^R u_0(r)J_0\left(\frac{kr\rho}{f}\right)rdr=\sum_{n=1}^{N}\int_{r_{n-1}}^{r_n}(-1)^n J_0\left(\frac{kr\rho}{f}\right)rdr\\
&=\sum_{n=1}^{N}(-1)^n\left(\frac{f}{k\rho}\right)^2\left[tJ_1(t)\right]\Big|_{k\rho r_{n-1}/f}^{k\rho r_n/f},\quad t=k\rho r/f\\
&=\sum_{n=1}^{N}(-1)^n\left[r_n^2\frac{J_1(k\rho r_n/f)}{k\rho r_n/f}-r_{n-1}^2\frac{J_1(k\rho r_{n-1}/f)}{k\rho r_{n-1}/f}\right]\\
&=f^2\sum_{n=1}^{N}(-1)^n\left[\sin^2\theta_n\frac{J_1(k\rho\sin\theta_n)}{k\rho\sin\theta_n}-\sin^2\theta_{n-1}\frac{J_1(k\rho\sin\theta_{n-1})}{k\rho\sin\theta_{n-1}}\right]\\
&=f^2\left[(-1)^N\sin^2\theta_N\frac{J_1(k\rho\sin\theta_N)}{k\rho\sin\theta_N}\right.\\
&\quad\left.+2\sum_{n=1}^{N-1}(-1)^n\sin^2\theta_n\frac{J_1(k\rho\sin\theta_n)}{k\rho\sin\theta_n}\right]
\end{aligned}, \tag{3.13}$$

where the incident beam is uniform and modulated by an N-belt binary phase such that $u_0(r)=\exp[i\varphi(r)]$, with $\varphi(r)=0$ or $\varphi(r)=\pi$ corresponding to different ranges of the radius r; $\sin\theta_n=r_n/f$ for the focusing lens satisfies the sine condition; θ_n is the focusing angle, where $\theta_0=0$ and the maximum angle is $\theta_N=\sin^{-1}(\mathrm{NA})$, as indicated by Eq. 3.6. Interestingly, Eq. 3.13 provides an analytical model for approximating the electric field in the focal region, and the time-consuming integral is not involved. Using Eq. 3.13, we can obtain an arbitrary intensity pattern by varying the unknown parameter θ_n (n=1, 2, …, N-1).

A factor D was used to describe the dimension of the flattened regime in Figure 3.13. When D becomes extremely large and the magnitude therein is completely smeared out, then the AR PSF can be achieved. Here, the factor D is applied to quantitatively describe the AR imaging capability.

The AR PSF has zero intensity at $\rho=0$ (suppressing the main-lobe intensity), an intensity approaching zero in the range $0<\rho<\mathrm{D}/2$ (widening the main lobe) and the largest intensity in the side lobe (enhancing the side lobe). To achieve the goal of suppressing the main-lobe intensity in AR, the intensity can be set to zero at $\rho=0$, leading to the equation

$$(-1)^N \sin^2\theta_N + 2\sum_{n=1}^{N-1}(-1)^n \sin^2\theta_n = 0. \tag{3.14}$$

In Eq. 3.14, the N-1 unknown parameters θ_n (n=1, 2, …, N-1) represent the infinite number of solutions that can achieve the goal of suppressing the

main lobe, which implies the possibility of these solutions being reduced to only one solution if more constraints are imposed on Eq. 3.14, e.g., reserving N-2 zero-intensity locations in the region $0<\rho<D/2$ to widen the main lobe (the secondary goal of AR). To achieve the third goal of enhancing the side lobe, no further measures are necessary because from the perspective of energy conservation, a high side lobe is the natural result of the near-zero intensity in the range $0\leq\rho<D/2$. Therefore, it is physically feasible to construct an AR PSF. In fact, the zero intensity in the region $0\leq\rho<D/2$ that is shown in Figure 3.22 is primarily attributed to the local destructive interference caused by the 0-π phase modulation of the BOE.

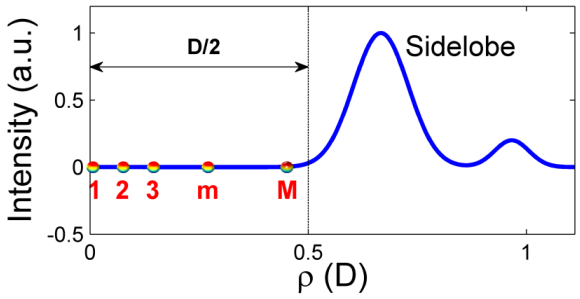

Figure 3.22. The radial (along ρ) pattern of the AR PSF [Appendix B 1]. The prescribed positions from 1 to **M** (**M**=**N**-1) in the range $0\leq\rho<D/2$ are indicated by the colored spots and located in the zero-intensity region of the intensity line (blue).

For convenience of demonstration, we simplify Eq. 3.13 using certain characteristic functions and extend the optimization-free method [91] to the AR case:

$$A(\rho)=(-1)^N \sin^2\theta_N \frac{J_1(k\rho\sin\theta_N)}{k\rho\sin\theta_N}, \tag{3.15}$$

$$B(\theta_n) = 2\cdot(-1)^n \sin^2\theta_n, \tag{3.16}$$

$$C(\rho,\theta_n) = \frac{J_1(k\rho\sin\theta_n)}{k\rho\sin\theta_n}. \tag{3.17}$$

By doing so, we obtain

$$U(\rho) = A(\rho) + \sum_{n=1}^{N-1} B(\theta_n) C(\rho,\theta_n), \tag{3.18}$$

without the constant f^2 that appears in Eq. 3.13. Based on the above discussion, in addition to the central position ρ=0, we still must prescribe N-2 zero-intensity positions in the region 0<ρ<D/2; these are indicated by the points labeled from 2 to M in Figure 3.22. The prescribed zero-intensity positions are labeled with the index m (m=1, 2, …, M) to distinguish this notation from the belt label n; as a result, the prescribed zero-intensity positions are labeled as ρ_m (m=1, 2, …, M). According to Eq. 3.18, we have the following M equations for these M positions:

$$\begin{aligned}
&A(\rho_1)+B(\theta_1)C(\rho_1,\theta_1)+B(\theta_2)C(\rho_1,\theta_2)+\cdots\\
&\quad +B(\theta_n)C(\rho_1,\theta_n)+\cdots+B(\theta_{N-1})C(\rho_1,\theta_{N-1}) = U(\rho_1)=0\\
&A(\rho_2)+B(\theta_1)C(\rho_2,\theta_1)+B(\theta_2)C(\rho_2,\theta_2)+\cdots\\
&\quad +B(\theta_n)C(\rho_2,\theta_n)+\cdots+B(\theta_{N-1})C(\rho_2,\theta_{N-1}) = U(\rho_2)=0\\
&\qquad\qquad\qquad\qquad\qquad\qquad\qquad\qquad\qquad\vdots\\
&A(\rho_m)+B(\theta_1)C(\rho_m,\theta_1)+B(\theta_2)C(\rho_m,\theta_2)+\cdots\\
&\quad +B(\theta_n)C(\rho_m,\theta_n)+\cdots+B(\theta_{N-1})C(\rho_m,\theta_{N-1}) = U(\rho_m)=0\\
&\qquad\qquad\qquad\qquad\qquad\qquad\qquad\qquad\qquad\vdots\\
&A(\rho_M)+B(\theta_1)C(\rho_M,\theta_1)+B(\theta_2)C(\rho_M,\theta_2)+\cdots\\
&\quad +B(\theta_n)C(\rho_M,\theta_n)+\cdots+B(\theta_{N-1})C(\rho_M,\theta_{N-1}) = U(\rho_M)=0
\end{aligned}, \tag{3.19}$$

which can be simplified to

$$\mathbf{CB} = \mathbf{A}, \tag{3.20}$$

where **C** is an M× (N-1) matrix with elements $C_{mn} = C(\rho_m,\theta_n)$, **B** is an (N-1)×1 matrix with elements $B_n=B(\theta_n)$, and **A** is an M×1 matrix with elements $A_n = -A(\rho_m)$. Eq. 3.20 is a non-linear matrix equation because **C** and **B** are dependent on the unknown parameters θ_n. In Eq. 3.20, the number of unknown parameters and the number of equations are the same, and therefore, there is only one solution. For the special position $\boldsymbol{\rho}=[\rho_1, \rho_2, \ldots, \rho_M]$, which depends on the customized requirement on the size of D illustrated in Figure 3.22, we can solve the non-linear equation represented by Eq. 3.20 to finalize the design of the binary phase element by fixing the angles $\theta_n(n=1, 2, \ldots, N-1)$. Unlike a linear matrix equation, the non-linear matrix equation in Eq. 3.20 cannot be solved using the simple matrix-inversion technique, which is commonly used to solve linear matrix equations. In fact, a non-linear matrix equation generally has no analytical solution, but its numerical solution can be straightforwardly obtained using the well-developed Newton's method, which is often applied in related engineering problems [92, 93]. In addition, specialized packages for solving non-linear matrix equations are also available in some commercial computing software, e.g., MATLAB and Mathematica. Therefore, the solution of Eq. 3.20 is not a troublesome issue. Sometimes, for one special position **ρ** **(**e.g., when ρ_m and ρ_{m+1} are too close**)**, the mathematical solution to Eq. 3.20 that is provided by Newton's method may not be a physical solution, in which case it must be rejected. For a solution to be physical, it must satisfy the following condition: $0<\sin\theta_n <\sin\theta_N$.

a

No.	r_1	r_2	r_3	r_4	d_0	NA
1	0.2929	0.5648	0.7914	0.9451	$1.022\times10^5\lambda$	0.0075
2	0.2860	0.5543	0.7828	0.9420	$1.030\times10^5\lambda$	0.0075
3	0.2769	0.5402	0.7706	0.9373	$1.043\times10^5\lambda$	0.0075
4	0.2664	0.5231	0.7546	0.9308	$1.075\times10^5\lambda$	0.0075

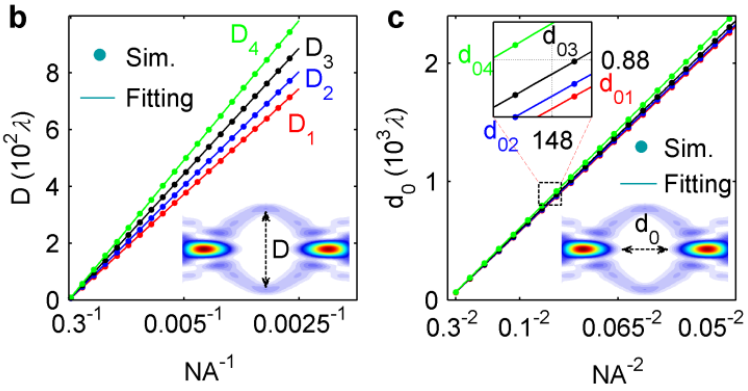

Figure 3.23. The ring belts design and its scaling properties of optical capsule for the lens with different NA [Appendix B 1]. (a) Four sets of parameters that demonstrate the robust design of super-sized AR-based cloak by the optimization-free method. (b) The radial size (D) of null field in optical capsule generated by the lens with different NA (from 0.3 to 0.0025) and the four sets of binary-phase plates in (a). Their fitting curves for different cases are: D_1=1.8600λ/NA for No.1 set of ring belt, D_2=2.0117λ/NA for No.2, D_3=2.2171λ/NA for No.3 and D_4=2.4605λ/NA for No.4. All the four cases, the root-mean-square errors (RMSE) between the original data and fitting curves have an order of magnitude 10^{-14}, indicating a perfect proportion of radial size D to 1/NA. (c) The axial size (d_0) of null field in optical capsule generated by the lens with different NA (from 0.3 to 0.05) and four sets of binary-phase plates in (a). Their corresponding fitting curves are d_{01}=5.7728λ/NA^2, d_{02}=5.8170λ/NA^2, d_{03}=5.8944λ/NA^2 and d_{04}=6.0762λ/NA^2 with their fitting RMSEs at the order of magnitude 10^{-12}, implying that the axial size d_0 is proportional to 1/NA^2.

In Figure 3.23a, four sets of binary phase plates designed using Eq. 3.20 to generate AR PSFs are shown. We chose the zero-intensity position at **ρ**=[0, 22.5 μm, 45 μm, 67.5 μm, 90 μm] as No. 1, that at **ρ**=[0, 27.5 μm, 75 μm, 82.5 μm, 110 μm] as No. 2, that at **ρ**=[0, 32.5 μm, 65 μm, 97.5 μm, 130 μm] as No. 3 and that at **ρ**=[0, 37.5 μm, 75 μm, 112.5 μm, 150 μm] as No. 4. The

NA of the focusing lens was fixed to 0.0075 for the design of these four sets of binary phase plates. The data are presented in Figure 3.23a.

3.4 Generation of an electromagnetic null field based on the AR PSF

In the previous section, we introduced the design of a binary phase element for realizing the AR PSF. Now, we will explain the physical mechanism of the generation of the electromagnetic null field when the AR PSF is achieved at the focal plane [Appendix B 1].

First, we revisit the different focusing behaviors along the transverse and axial directions of a lens. Without loss of generality, we analyze the intensity at the focal plane $z=f$ for the transverse direction and the on-axis intensity at $r=0$ for the axial direction. For uniform illumination without the imposition of any phase or amplitude modulation by binary elements, we can use Eq. 3.12 to find the intensities at $z=f$ and $r=0$ in analytical form:

$$I(\rho, z=f)=\left|\int_0^R J_0\left(\frac{kr\rho}{f}\right)rdr\right|^2=R^4\left[\frac{J_1(k\rho R/f)}{k\rho R/f}\right]^2, \tag{3.21}$$

$$I(\rho=0, z)=\left|\int_0^R e^{\frac{ikr^2}{2z}}e^{-\frac{ikr^2}{2f}}rdr\right|^2=\frac{R^4}{4}\left\{\frac{\sin\left[R^2k\left(\frac{1}{z}-\frac{1}{f}\right)\right]}{R^2k\left(\frac{1}{z}-\frac{1}{f}\right)}\right\}^2, \tag{3.22}$$

where $I(\rho,z=f)$ and $I(\rho=0,z)$ represent the intensity profiles at the focal plane and on the axis at $\rho=0$, respectively. From Eqs. 3.21 and 3.22, we can

determine the size (from the focal point to the first zero-intensity point) in both the radial and axial directions. For the radial size at the focal plane, the first zero-intensity point is located at $k\rho R/f$=3.8317, which implies a radial size of

$$\Delta\rho = \frac{0.61\lambda}{NA}, \tag{3.23}$$

where NA≈R/f for a low-NA lens, as demonstrated by Figures 3.24a and 3.24b. For the axial size at ρ=0, the first zero-intensity point is located at $R^2k(1/z\text{-}1/f)=\pi$, which implies an axial size (Figures 3.24a and 3.24c) of

$$\Delta z = \left|\frac{\lambda}{\lambda/f + 2(R/f)^2}\right| \approx \frac{0.5\lambda}{NA^2}. \tag{3.24}$$

From the radial and axial sizes given by Eqs. 3.23 and 3.24, it is apparent that the radial size is proportional to 1/NA, whereas the axial size is proportional to 1/NA^2. Because the NA of the lens is smaller than 1, the size of the spot in the radial direction is smaller than that in the axial direction, as shown in Figure 3.24, which indicates that the focusing lens provides tighter confinement in the radial direction than in the axial direction. This is a very important and fundamental conclusion in the field of the optical focusing of lenses. Therefore, for a well-constructed AR PSF at the focal plane, based solely on this physical conclusion and without further investigation of the intensity distribution in the axial region, we can intuitively predict that the zero-intensity region in the axial direction for ρ=0 must be much larger than that in the radial direction.

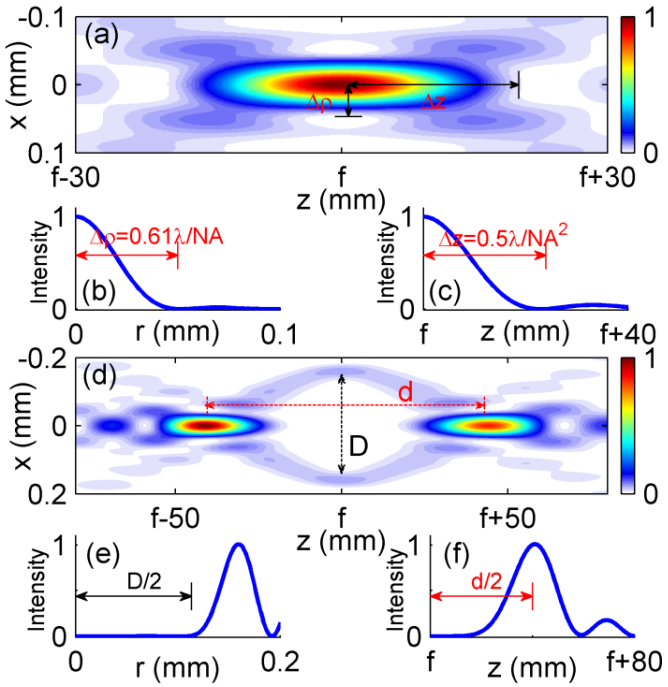

Figure 3.24 The focusing properties of a lens [Appendix B 1]. (a) The intensity profile on the *xz* plane of the focusing field of a lens. (b) The radial intensity profile of the focused spot on the focal plane depicted in (a). (c) The axial intensity profile at ρ=0 as depicted in (a). (d) The intensity profile of the optical capsule in the focal region of a lens and a binary phase plate. D and d are the radial and axial sizes (from one hotspot to another), respectively, of the optical capsule. (e) The radial intensity profile of the optical capsule on the focal plane depicted in (d). (f) The axial intensity profile of the optical capsule at ρ=0 as depicted in (d).

Because the above theoretical prediction describes the mechanism of the generation of the electromagnetic null field by means of the AR PSF, we confirmed the above prediction through analytical simulations based on Eq. 3.12. In fact, the simulation results presented in Figures 3.23b and 3.23c confirm the prediction that the transversal (D) and axial sizes (d_0) should be proportional to 1/NA and $1/NA^2$, respectively. Because NA<1, the axial size d_0 is always larger than the transversal size D. Although the simulations presented in Figure 3.23c already provide an unquestionable verification of the

existence of the axial null field, we can also find physical proof of its existence in the uniform variation of the energy flux of light in a homogenous medium. In the previous section, we demonstrated the generation of the AR PSF with the null-field region $0 \leq \rho < D$ on the focal plane. If we move the viewing position to an out-of-plane ($z \neq f$) position, we can predict the existence of a null field at this out-of-plane position because of the uniform variation in the energy flux of light in air, as shown in Figure 3.24d. This null-field region will exist until the out-of-plane position is moved beyond one of the two ends of the null field. Because the axial confinement of the focusing lens is much weaker than the transversal confinement, as indicated by Eqs. 3.23 and 3.24, the null field extends farther in the axial direction than in the transversal direction. Therefore, an electromagnetic null field with widely separated boundaries in the axial direction and narrowly separated boundaries in the transversal direction is formed when an AR PSF is generated at the focal plane.

3.5 Summary

In this chapter, we focused primarily on the new phenomenon of AR in the focal region. First, to lay the theoretical foundation, the focusing properties of a radially polarized CV beam were discussed. Based on the Richards-Wolf's vector diffraction theory, which was derived in Chapter 2, the field distribution was obtained. It was found that the energy is primarily concentrated in one

wavelength region near the focus. Although there is a strong longitudinal component, the beam purity is low, and less than 46% of the beam is oriented in the propagation direction.

Subsequently, the abnormal distribution of a non-diffracted beam was investigated to confirm the influence of a BOE on the electric field. A uniform distribution with a length of 4λ was obtained. The beam purity is improved significantly in this case, and approximately 80% of the total energy near the axis is generated by the longitudinal field.

Third, all these results were applied to the phenomenon of AR generation. A new optical system composed of a BOE and a focusing lens was designed. By comparing the physical model with the requirements for AR, the three-dimensional problem was transformed into a simpler one. After we obtained the parameters for the diffractive phase mask through optimization, we investigated the field distributions and demonstrated the creation of the desired profile, as predicted in the model. The same methodology is also valid for azimuthally polarized incident light.

In order to design a BOE to realize the AR PSF, a generalized methodology referred to as an optimization-free method based on the physical concept was then proposed. The problem was quantitatively described in terms of an explicit mathematical model. By solving the non-linear matrix equation, through the well-developed Newton's method, the parameters of the BOE can be obtained.

Finally, the physical reason for the generation of an electromagnetic null field was explained in low-NA systems. The simulation results suggested that the AR PSF can be realized in this case and that the volume of the three-dimensional electromagnetic null field is proportional to λ/NA^3.

As a new optical phenomenon, AR holds promise for a large number of important applications. It can be used for surveillance, as it can allow light to be bent around a macroscopic object, thereby permitting the detection of another object placed behind it. In addition, this novel technology also establishes a new approach to future applications in large-scale trapping, atom cooling and particle manipulation.

Chapter 4

Macroscopic electromagnetic cloaking in an imaging system

4.1 Introduction

Since Pendry and Leonhardt individually established transformation optics theory [26, 94], a number of novel electromagnetic phenomena have been observed and have motivated many interesting applications [95, 96]. Among these, invisibility cloaking has attracted the most attention, as many significant applications can be conceived with it. Meanwhile, it broadens our minds to imagine a world in which objects can be made invisible in space [97-111]. The application of transformation optics theory for cloaking relies on the specific design of the electromagnetic parameters of materials or the application of metamaterial structures. By this means, all incoming waves are guided to propagate around a shell-like region without interacting with the object located

inside. This specially designed shell is called a free-space invisibility cloak and is illustrated in Figure 4.1.

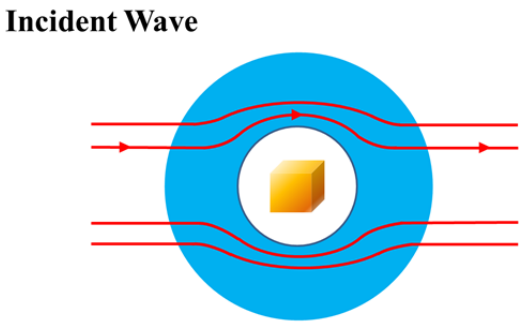

Figure 4.1 Schematic illustration of transformation-optics cloaking. The incident wave is bent and passes through the cloaking region without touching the object lying inside.

Despite the large variety of cloaks that have been designed and analyzed theoretically, because the extreme requirements on the electric permittivity and magnetic permeability of the materials, the realization of a free-space cloak poses a considerable challenge to modern fabrication technologies. Meanwhile, the existing reduced cloak at microwave frequencies offers unsatisfactory performance. To overcome this difficulty, a fully dielectric carpet cloak, based on quasiconformal mapping, has been proposed by Li and Pendry (illustrated in Figure 4.2) [112]. In this cloaking mechanism, objects can be hidden under a ground plane covered by the cloaking metamaterial. In the design of such a ground-plane cloak, singular values do not exist in the material parameters, and exciting experimental results have been achieved at microwave, terahertz and optical frequencies [113-117]. Unfortunately, it has recently been found that a lateral shift in the scattered wave, which is comparable to the height of

the hidden object, can be produced by a quasiconformal-mapping-based carpet cloak, and this shift will certainly allow the object to be detected [118].

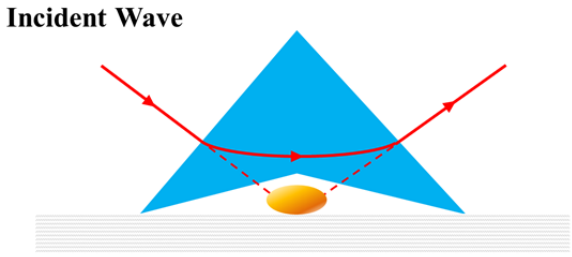

Figure 4.2 Schematic illustration of carpet cloaking. A wave is incident from the left and passes through the cloaking region without touching the object lying on the ground.

To overcome the defects and limitations of the carpet cloak, such as situations in which the object it should be concealing is detectable and its complicated fabrication, a natural-crystal-based macroscopic cloak has recently been reported [119-122]. In contrast with all previous cloaking methods, which depend on sharp coordinate transformation, this macroscopic cloaking approach makes full use of the birefringent property of calcite. A linear homogeneous transformation can therefore satisfy the requirements. Although low-cost material is utilized, there are still some problems to be solved before this cloaking technology can be put into practice. Considering a recent study as an example (shown in Figure 4.3), the triangle of height H_1 and half-width d stands for the cloaked region (Figure 4.3b); H_2 represents the height of the natural crystal. According to transformation optics theory, the relation among H_1, H_2 and d is [119]

$$\frac{H_1}{H_2}=1-\sqrt{\frac{n_o^2\sin^2\gamma+n_e^2\cos^2\gamma}{n_o^2\cos^2\gamma+n_e^2\sin^2\gamma}-\left(\frac{H_1}{d}\right)^2}\,, \tag{4.1}$$

where γ is the angle between the optical axis of the calcite and the y axis and where n_o and n_e represent the refractive indices of ordinary and extraordinary light, respectively. Because of the small anisotropy of a natural crystal (for calcite, n_o-n_e=1.66-1.49=0.17) and its limited size in nature (usually several centimeters), the size of the cloaked region is typically only a few millimeters.

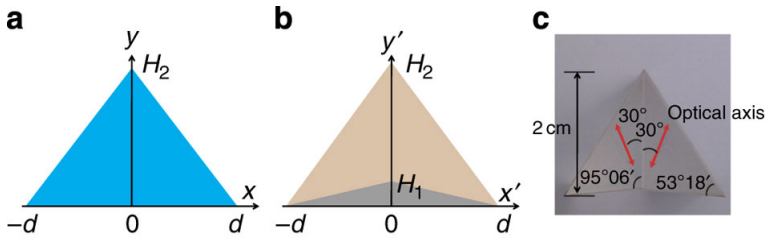

Figure 4.3. Schematic illustration of macroscopic invisibility cloaking at visible frequencies. This figure is reprinted from [119]. Reprinted with permission from Nature Publishing Group.

Based on the discussion above, the key mechanism underlying all transformation-optics cloaking technology is the guiding of waves to a desired path while avoiding interactions between the waves. Most efforts thus far have focused on the question of how to acquire the specific materials and structures necessary to achieve this feat.

As discussed in previous chapters, a low-intensity field distribution can be numerically and experimentally created for particle trapping and manipulation. When this type of field illuminates an object, then the scattering from the object, which is the basis for imaging in practical applications, will

be extremely weak and difficult to detect. This phenomenon of low-intensity fields provides the possibility of realizing the "light capsule" necessary for cloaking. However, in previous works, the null-field-distribution region of this phenomenon has generally been limited to a single point. Because an object placed in such a low-intensity region must have a finite volume, there will still be interactions between the object and the incident waves. Thus, the object will certainly be detected because of its influence upon the incident wave.

In Chapter 3, we investigated the new phenomenon of AR in the focal region. Because the PSF of the optical system vanishes in a certain region, a large null-field region surrounded by visible light is therefore achieved. Any object placed in this region cannot be resolved. Here, we report a novel macroscopic electromagnetic cloaking method using an imaging system based on AR. This novel scheme overcomes the limitations of conventional transformation-optics-based cloaking and quasiconformal-mapping-based carpet cloaking, including narrow bandwidths, polarization restrictions, and metamaterial requirements. In AR-based cloaking, which consists of conventional BOEs and focusing lenses, a null-field region is created by precisely tailoring the interferences of a large number of beams diffracted from the BOEs.

4.2 Macroscopic electromagnetic cloaking design and its performance

4.2.1 Macroscopic electromagnetic cloaking design

Imaging theory has taught us that once an object is placed in the focal region of a system, it will be resolved and detected easily. Traditionally, the PSF of an optical system is narrowed to be as sharp as possible to enhance the imaging resolution. Once the distance between two points becomes sufficiently narrow to exceed the diffraction limit ~λ/2NA, these two points can no longer be distinguished. Nevertheless, it is still possible to be certain of the existence of the unresolvable object because of the influence it exerts on the optical environment. To hide an object in an optical system, it is necessary to achieve an electromagnetic null-field region instead of a sharp focus. In contrast to super-resolution, which makes an object highly resolvable, AR stably causes the object to become unresolvable when exposed to an extremely low-frequency electromagnetic field. As shown in Chapter 3, this specific electromagnetic field can be created by employing a BOE. In this manner, we can ensure that the light will pass through a certain area and produce the desired null field.

Before explaining the theoretical mechanism of this macroscopic cloaking technology, we will first present the full structure of its physical realization [Appendix B 1] . A schematic diagram of the entire cloaking device

is presented in Figure 4.4. A radially polarized Bessel-Gaussian beam, which is used in the attempt to detect the object, propagates from left to right and passes through two pairs of specially designed diffractive phase masks and focusing lenses. For convenience, the parameters of the elements used here are those derived for generating AR in Chapter 3. The optical system consists of two types of elements, each of which will affect the cloak in a different manner. To generate Figure 4.4, we chose a focusing lens with NA=0.95. According to the simulation results and previous discussions, when we fix the lens parameters, the area of the null field will be restricted to a certain range.

After passing through the first pair of specially designed phase-mask elements and focusing lens, the light propagates along the curve shown in Figure 4.4 and creates a perfect dark region where the field intensity approaches zero. This is the AR phenomenon achieved in Chapter 3. When we investigate the field distribution on the optical axis, we note that the intensity is zero over a certain distance, as shown in the inset of Figure 4.4. This specific field distribution and wave-propagation behavior ensure that there are no interactions between the light and the object. Moreover, we know that for effective electromagnetic cloaking, the incident wave and the output wave must both contain the same information, and it is therefore necessary to rebuild the wavefront to avoid any difference between them. When previous cloaking schemes are analyzed, it is apparent that their structures are symmetric with respect to the reference plane. Interestingly, the phenomenon

of AR itself is also symmetric, so an identical pair of a lens and a complementary phase mask is positioned symmetrically on the other side of the focal point to restore the phase front of the incident beam. It should be noted that this system has been confirmed to be suitable for a large variety of types of incident light, e.g., plane waves and Bessel-Gaussian beams. To explore the methodology, we first suppose that the field at the exit pupil of the focusing lens is a radially polarized CV beam.

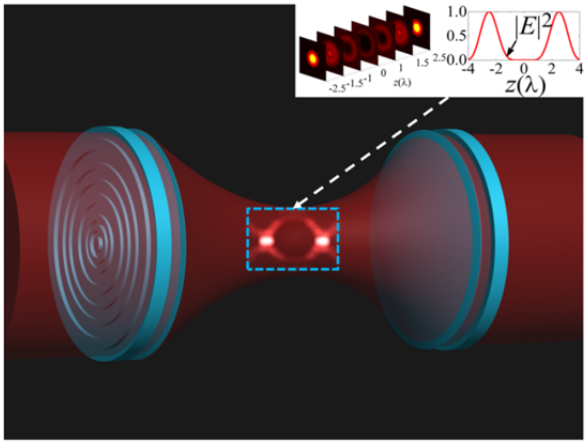

Figure 4.4 Physical configuration and field distribution of an AR-based cloaking system [Appendix B 1]. A Bessel-Gaussian beam propagates through two specially designed pairs of diffractive phase masks and focusing lenses from left to right. The inset shows the magnitude of the total electric field along the optical axis, in which a nearly perfect null region (the field amplitude is on the order of 10^{-5}) is formed. Seven cut planes at equal separation distances are depicted to illustrate the individual transversal field intensities.

4.2.2 Simulation results of AR-based cloaking

To verify the design of the AR-based cloaking device, we place an object in the cloaking region and test its performance [Appendix B 1]. Using exactly the

same phase-modulation mask and focusing lens shown in Figure 4.4, we consider radially and azimuthally polarized incident light (Figures 4.5a and 4.5b, respectively). In Figures 4.5a and 4.5b, the electric-field distributions are depicted; it is evident that the three-dimensional AR regions appear within an area of approximately the same size in each case. One important factor in the cloaking is the energy change that occurs when the object is introduced.

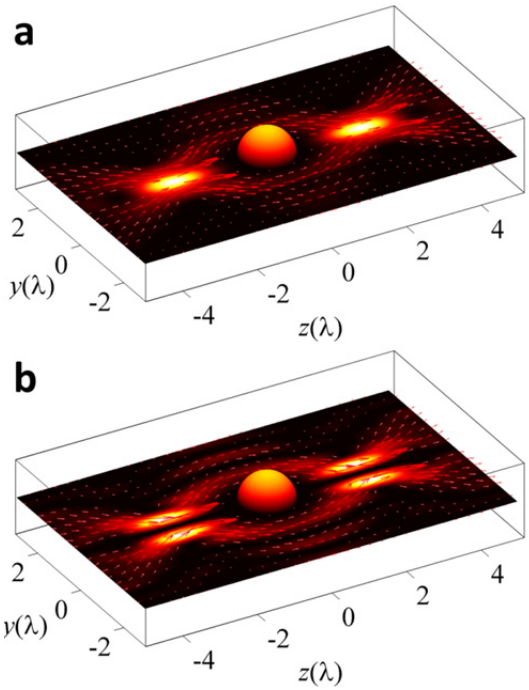

Figure 4.5. Full-wave simulations of the energy-flux bifurcation and reformation in an AR-based cloaking system with NA=0.95 [Appendix B 1]. (a) The incident light is radially polarized. (b) The incident light is azimuthally polarized. A metallic sphere with a radius of one wavelength is placed in the center.

Therefore, full-wave simulations of the Poynting vector field

$$\boldsymbol{S} = \frac{c}{4\pi}\mathrm{Re}\left(\boldsymbol{E}\times\boldsymbol{H}^{*}\right) \tag{4.1}$$

are used to verify that the energy in the AR region is negligible when an object of one wavelength in radius is placed in the AR region (the size of the object was chosen in accordance with the size of the AR region). The bifurcation and reformation of the energy flux unambiguously demonstrate that the performance of the AR-based cloaking device is insensitive to the polarization state of the incident light. Hence, any complex polarization state that is a vector superposition of radial and azimuthal polarizations will yield a perfect AR effect and cloak the object within the null-field region.

In principle, the volume of the nearly perfect null-field region that can be created is unlimited, and hence, macroscopic electromagnetic cloaking is possible. It was found in Chapter 3 that the size of the AR region (the null field) can be significantly enlarged by reducing the NA value of the focusing lens ($\sim 1/\mathrm{NA}^3$) and that regardless of the NA value used, the AR region is consistently created and cloaking is consistently achieved in the imaging system. When the phase mask is held invariant and the lens in Figure 4.4 is replaced by one with a lower NA (e.g., NA=0.01 or NA=0.001), the axial and transversal null-field regions can be enlarged to approximately $4\times10^4\lambda$ and $4\times10^2\lambda$, respectively, when NA=0.01 (as shown in Figure 4.6a) or to $4\times10^6\lambda$ and $4\times10^3\lambda$, respectively, when NA=0.001 (as shown in Figure 4.6b). If the operating frequency is in the microwave (terahertz) range, a region of this size is meaningful in practice. Both cases illustrated in Figure 4.6 have proven to be robust for both radially and azimuthally polarized light, which is important

for handling incident light of arbitrary polarization status.

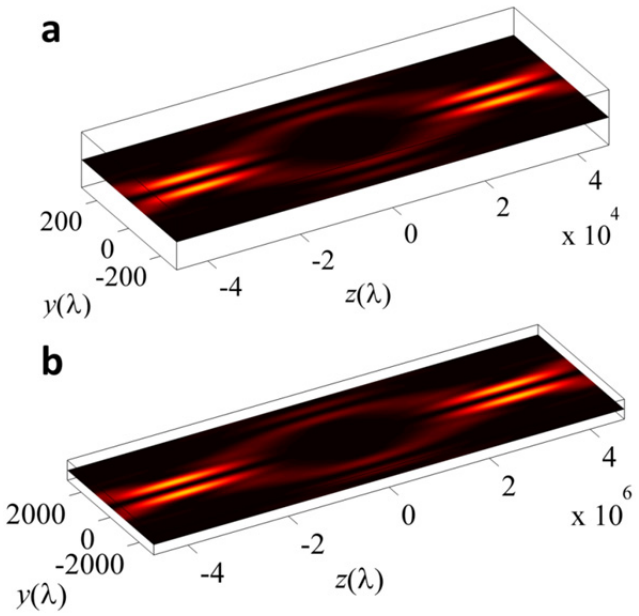

Figure 4.6. Electric-field distributions in AR-based cloaking. A radially polarized Bessel-Gaussian beam is used as the incident wave. (a) The NA of the focusing lens is 0.01. (b) The NA of the focusing lens is 0.001.

4.2.3 Mechanism of AR-based cloaking

In modern optical systems, three major phenomena of light are typically utilized: reflection, refraction and diffraction. AR cloaking utilizes a field distribution based on the diffraction effect in the focal region. In addition to the specific intensity distributions, other properties, such as the polarization and phase of the focused beam, also have various manifestations in the focal region. Recently, the wavefront spacings of a focused linearly polarized beam and a radially polarized beam have been investigated by Foley and Visser, respectively [123, 124]. A significant difference between the two cases was observed, and the principle behind this difference is the Gouy phase shift,

which was discovered a century ago. Because the phenomenon of light bending and null-field formation based on AR are so attractive, it is necessary to reveal the underlying physics of the AR phenomenon. Here, we present Figures 4.7 and 4.8 to elucidate the fundamental mechanism driving the evolution of the null field in Figure 4.4, namely, the size variation of the blind spots along the propagation direction [Appendix B 1].

As shown in Figures 4.7 and 4.8, the electric field on the beam axis ($r = 0$) is purely longitudinally polarized (E_z is the only electric-field component). Because this polarization is parallel to the direction of light propagation, at first glance, it seems to violate Maxwell's equations governing the propagation of electromagnetic waves. Nevertheless, when the position deviates from the beam axis ($r \neq 0$), a radial component E_r begins to emerge, as indicated by Figure 4.4, which plays an important role in enabling the light to propagate, bend and reach the second focus.

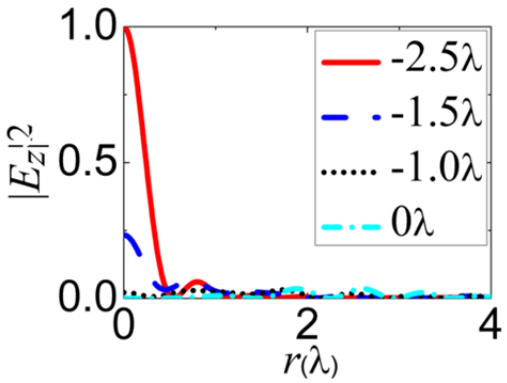

Figure 4.7. Electric-field distribution of the AR system on the xy plane (z=0) [Appendix B 1]. The longitudinally polarized field intensities on the first 4 transversal cut planes are presented in Figure 4.4. The cut plane at $z = 0\lambda$ corresponds to the middle plane between the first focus ($z = -2.5\lambda$) and the second focus ($z = 2.5\lambda$).

At $z = -2.5\lambda$ (the first imaging plane), E_z clearly dominates within the region near the beam axis ($r < 0.2\lambda$), and the wave is therefore prohibited from propagating straight along the beam axis and instead must travel in a curvilinear trajectory. At $z = 0\lambda$ (between the two imaging planes), Figure 4.8 shows that E_r (corresponding to the propagation) is nearly smeared out within the central region around the beam axis. At greater deviation from the center axis, E_r gradually arises, and this component corresponds to both the propagation and the first colored ring in the cut plane at $z = 0\lambda$ in Figure 4.4.

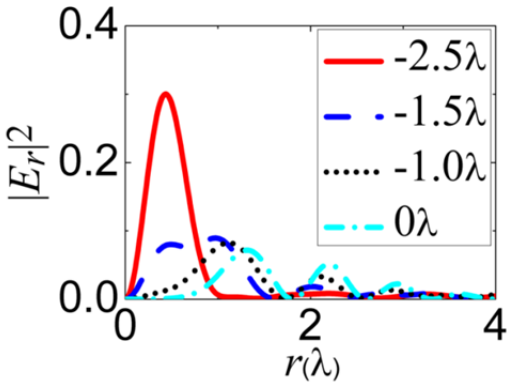

Figure 4.8. Electric-field distribution of the AR system on the xy plane ($z = 0$) [Appendix B 1]. The radially polarized field intensities on the first 4 transversal cut planes are presented in Figure 4.4. The cut plane at $z = 0\lambda$ corresponds to the middle plane between the first focus ($z = -2.5\lambda$) and the second focus ($z = 2.5\lambda$).

4.3 Experiments of AR-based cloaking

To verify the simulation results and our model, we experimentally demonstrate this novel phenomenon of the bifurcation and reformation of light in free space, i.e., AR-based invisibility [Appendix B 1]. There are two results of

interest in such an experiment. As it is the basis of AR-based cloaking, an electromagnetic null-field distribution is the first goal. Once this phenomenon of AR is observed, the disturbance caused by placing an object in the null-field region should be the second factor on which to evaluate the cloaking performance.

The experimental setup is depicted in Figure 4.9. A pupil comprising an opaque gold circular disk (150 μm in diameter) is placed at the center of the AR region to block the straight line of sight and to serve as the object to be cloaked. A spatial light modulator (SLM) is employed to represent the equivalent phase modulation exerted by the diffractive phase mask and focusing lens of Figure 4.4. The phase-modulation mask consists of a phase-type spatial light modulator (HOLOEYE LC2002) with a pixel pitch of 32 μm for visible light. A small gap of approximately 8 μm in size exists between two neighboring pixels. When light that passes through this gap is focused by the lens, a spot will be generated at the focal plane of the focusing lens, regardless of the SLM phase.

Because a low-NA lens is equivalent to a lens phase of $\exp[-i\pi r^2/(f\lambda)]$ in Fourier optics, the low-NA lens in Figure 4.4 is replaced by an equivalent lens phase realized by the SLM. The experiment is conducted on an optical table of 3 meters in length. Because of the limited length of the optical table, we choose a focusing lens with an NA equal to 0.0048 and linearly polarized incident light with a wavelength of 532 nm. The laser is expanded by a beam

expander comprising two lenses and one pinhole of 10 μm in diameter. After passing through a stop with a diameter of 19.2 mm, the light illuminates the SLM, which simultaneously produces the phase mask and the lens phase with f=2 m. A mirror is used to alter the optical path to account for the limitation of the table length. An object is placed behind the pupil, and the distance between the pupil and the object is 20 mm. A CCD camera (IDS UI-2240) with a 20× camera lens is used to record the field intensity.

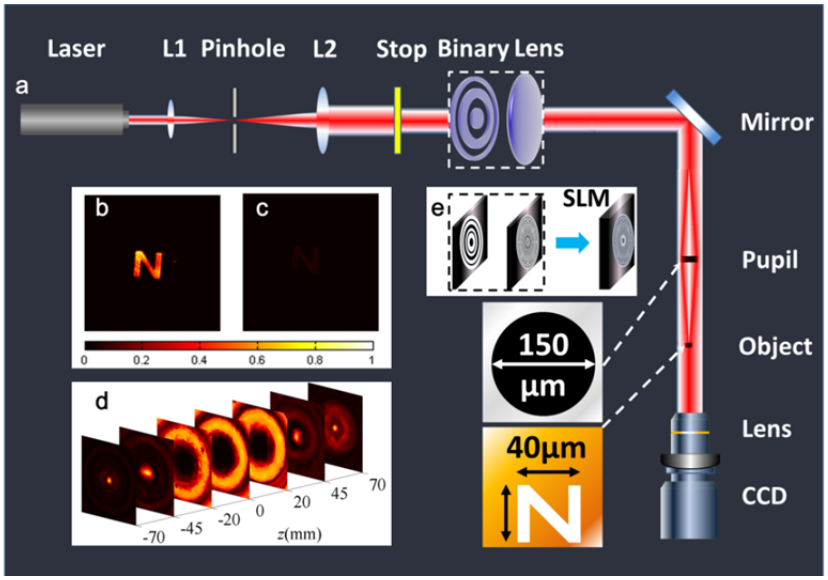

Figure 4.9. The experimental setup for the AR-based cloaking in the imaging system [Appendix B 1]. SLM adopts the phase profile from the theoretical calculation as shown herein. Three insets represent total phase profile (mask phase plus lens phase) implemented in SLM; the dimension of the opaque pupil as the object to be cloaked and the size of the letter beneath the object, respectively. (a) Schematic of the experiment. (b) When the mask phase and the lens phase are simultaneously adopted by SLM, light can bypass the opaque pupil and illuminate the object beneath. (c) When either mask or lens phase is adopted separately, the light is blocked by the opaque circular area. Almost no light can pass the pupil and a very dark "N" is captured by CCD. (d) Measured intensity on seven transversal planes, on both sides of the central plane (z=0). (e) The total phase profile of binary and lens is mimicked with SLM.

A gold plate with a letter 'N' etched through it is placed behind the pupil to confirm the reformation of the light bypassing the pupil. On the one hand, the imaging of the letter 'N' captured by the CCD camera in Figure 4.9a explicitly demonstrates that the light can bend and bypass a larger opaque pupil. On the other hand, when the phase mask is removed, the light is fully blocked by the opaque disk of the pupil, allowing only very limited light to reach the letter beneath the object. Consequently, a very dark "N" is captured by the CCD, as demonstrated in Figure 4.9b.

Such light bending and the creation of the AR region is further verified by the evolution of the transversal field patterns along the light-propagation direction at seven evenly distributed cut-planes between the first imaging plane (where the light is first split) and the second imaging plane (where the light is reformed), as shown in Figure 4.9d. It can be seen that a perfect null region forms with dimensions of approximately 0.3 mm ($\sim 5.6\times10^{2}\lambda$) in width and 40 mm ($\sim 7.5\times10^{4}\lambda$) in length, in good agreement with the theoretical calculations. In the meantime, within such a macroscopic AR region, the fields are perfectly smeared out such that the introduction of the macroscopic pupil causes little perturbation of the light that might cause it to bend or reform, as seen from Figure 4.9b. As discussed above, the transversal and axial sizes of the AR region are proportional to 1/NA and $1/NA^2$, respectively. Therefore, the size of the AR region may be extremely large and may even reach a value of $1.6\times10^{13}\lambda^2$ for an NA of 0.0001. The results of this experiment using an

SLM are in good agreement with the theoretical predictions and provide strong motivation for the realization of an AR-based cloak in a compact system.

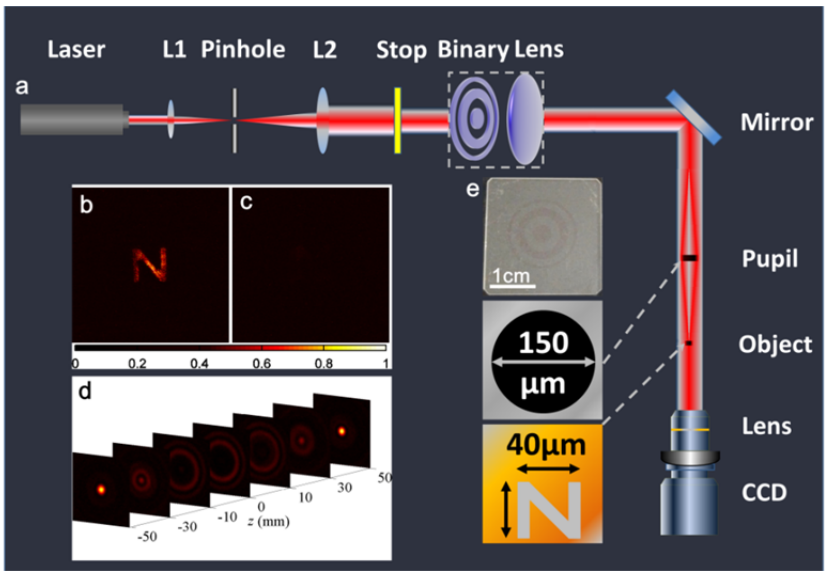

Figure 4.10. Controlled experiment when the binary mask is replaced with a spatial light modulator [Appendix B 1]. Experimental setup and measurement results for the AR-based cloaking enclose the super-size darkness region in the imaging system. (a) Schematic of the experiment. Two insets represent the dimension of the opaque pupil and the size of the letter beneath the object, respectively. (b) When the mask phase and the lens phase are simultaneously adopted, light can bypass the opaque pupil and illuminate the object beneath. (c) When either mask or lens phase is adopted separately (i.e., lens or 0-π modulation mask is removed), the light is blocked by the opaque circular area (150μm in diameter). Almost no light could pass the pupil and a very dark "N" is captured by CCD. A video (provided as a supplemental multimedia file) shows the switching of the bright and the dark "N", corresponding to situations of the presence and absence of 0-π mask phase. (d) Measured intensity on seven transversal planes, on both sides of the central plane (z=0). (e) The fabricated binary mask.

In an additional controlled experiment (shown in Figure 4.10), we use a binary phase mask fabricated on a quartz substrate. The wavelength of the incident light is 632.8 nm. The focusing lens has an NA of 0.0075 and a size

of 15 mm in diameter, which is the same as the stop size and the maximum diameter of the binary phase mask. The light passing through the groove has an additional phase difference of π compared with the light passing through the neighboring air belts. This additional π phase originates from their height difference of 692 nm, as the refractive index of quartz is 1.4507 at 632.8 nm. As seen from Figure 4.10b-4.10d, the same results are obtained here as in the previous experiment, in which the SLM serves as the BOE. Although this latter experimental setup requires time-consuming nanofabrication processes, it paves the way for practical cloaking in an imaging system and enables cloaking on the subwavelength scale.

4.4 Summary

Invisibility cloaking is currently being extensively studied for its potential uses in a broad variety of applications. Although the feasibility of this novel concept has been proven both in theory and in some experiments, there are still challenges to overcome before it will be suitable for practical applications. Existing cloaking schemes, such as carpet cloaking and birefringent cloaking, suffer from intrinsic limitations. In this chapter, we developed a novel scheme for electromagnetic cloaking by extending and employing the phenomenon of AR in an imaging system. The system is composed of two pairs of phase-modulation masks and focusing lenses. The effect of the first mask-and-lens pair is to form the AR field, and the light is then formed to

propagate along its original path after passing through the second pair. To verify our AR-based cloaking, two experiments were meticulously designed to investigate the field distribution and disturbance that could be achieved using this approach. From the results of these experiments, we determined that the bending of the light occurs on the macroscopic scale (three to six orders of magnitude larger than the wavelength), in dramatic contrast to the Airy beam that has recently been actively studied in plasmonics [125, 126]. Furthermore, there are no interactions between the probe light and the objects placed in the AR region. Although this method of cloaking is limited in terms of observation angles, it is free of a number of the constraints suffered by traditional invisibility cloaking, such as energy loss, narrow operation bandwidth, limited cloaking area, and polarization sensitivity.

Chapter 5

Conclusions

5.1 Conclusions

This thesis explored a newly discovered field distribution of focused CV beams. Based on the distribution in the focal region, an appealing concept, i.e., AR, was proposed along with its specifications. It was found that this novel phenomenon could be achieved by widening the field distribution infinitely to ultimately invert the PSF. This approach is in sharp contrast to the conventional super-resolution PSF in optics, which scientists and engineers have striven for years to narrow yet further through technical means. This unconventional distribution in the focal region can be primarily attributed to the reconstruction of the CV-beam wavefront. It was also found that the disturbance that arises when an object is placed in a field with such an AR distribution is invisible. These findings are important for focal optics because they offer a new approach to manipulating the shape of the focal region on the

subwavelength scale. Moreover, they contribute to a novel technology for cloaking in an imaging system.

The AR phenomenon was first identified in a tightly focused, radially polarized CV beam. To clearly demonstrate the realization of AR, Chapter 2 was devoted to introducing the CV beam and its focusing properties in a mathematical fashion. An accurate model of a tightly focusing system was achieved by finding mathematical solutions for beams with cylindrical symmetry, expressing the field in the focal region in terms of the Debye integral, and finally, extending the Richards-Wolf's vector diffraction theory to the general case. This field model is of crucial importance for focusing optics because it may assist in evaluating the performance of an optical system and guide its further improvement. Moreover, this model also provides an effective tool for investigating vortex and higher-order CV beams, which possess many peculiar properties.

As the primary objective of this thesis, the behaviors and properties of AR were investigated and demonstrated based on the mathematical model developed in Chapter 2. By focusing a radially polarized CV beam using a high-NA lens and a specifically designed BOE, the phenomenon of AR was achieved. It was found that the AR PSF leads to a ring-shaped intensity distribution that possesses a null field located in the center of the focal plane and spreads toward both sides of the focal plane. To design a BOE to produce the AR PSF, a generalized methodology referred to as an optimization-free

method based on the physical concept was employed. The problem was then quantitatively described in terms of an explicit mathematical model. In contrast with previous studies, which have employed fully developed algorithms (ant-colony optimization, simulated annealing algorithms), this optimization-free method represents a significantly different approach to the design of BOEs. In addition, this method enables us to solve the problem in a customized manner, hence tremendously improving computational efficiency. Finally, the AR phenomenon was verified in low-NA systems. The simulation results suggested that the AR PSF can also be realized in this case and that the volume of the three-dimensional electromagnetic null field is proportional to λ/NA^3. This finding implies the possibility of creating an extremely large null field, in principle, when NA is extremely small.

Based on the phenomena and results above, an AR-based cloaking model was also constructed in this study. It was found that any incident probe light will not interact with an object placed within the null region and will, instead, simply travel around the object. To investigate the properties of such an AR-based cloak, the Poynting vector was considered. It was found that the cloaking performance is almost entirely unaffected by the incident polarization state. Hence, any complex polarization states consisting of vector superpositions of radial and azimuthal polarizations will yield perfectly identical AR-based cloaking performances. To verify our theoretical model and test the simulation results, two experiments were then designed and

performed. The measurement results were in good agreement with the theoretical predictions. This cloaking technology is of considerable importance for realistic applications because the anisotropic materials and inhomogeneous structures that are required by traditional cloaking methods are unnecessary in the proposed scheme. Additionally, this method is immune from the polarization state of the incident light.

In summary, the major achievements reported in this thesis are as follows:

1) The proposal of the novel AR concept.

2) The design of a novel scheme based on AR for cloaking macroscopic objects under broadband illumination in a polarization-independent manner.

5.2 Recommendations for future work

In view of this interesting phenomenon of AR and its attractive applications, it is necessary to study its properties and further extend its usage. A direct extension of this work would be the application of AR in dark optical traps [127, 128]. As illustrated in Figure 5.1, if a particle is placed in a dark field within a background medium of a higher refractive index, the gradient force will be directed toward the lower-intensity region. This suggests that a field with an AR distribution can be used for trapping. Ideally, an electromagnetic field with a null central intensity distribution is desirable for this purpose. However, most previous efforts in this field have been based on low-intensity

fields instead of a null field, which we have clearly demonstrated in this thesis. Although the energy in the trapping center may be tiny, its influence is not negligible in comparison with the mass of the particle. The total field distributions have already been demonstrated in our discussions, and the light intensity in the central region can be further reduced by optimization for applications of atom cooling and particle manipulation. One benefit of the proposed optimization-free technique is that its contributions to the design of BOEs might be valuable for super-resolution imaging. Although the optimization-free method was proposed to achieve the AR PSF, with some modifications, it can also be used to design other distributions in the focal region, such as an optical needle and optical chain.

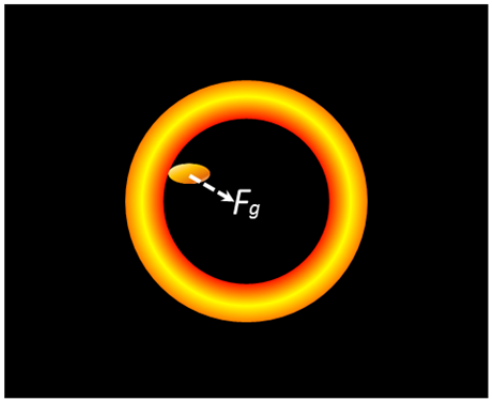

Figure 5.1 Schematic diagram of a dark optical trap. F_g represents the gradient force exerted on the particle. When the refractive index of the medium is higher than that of the particle, the gradient force F_g will be directed toward the lower-intensity region.

It is worth noting that the proposed cloaking scheme is effective only in one direction. Therefore, efforts should be made to extend the scheme to two-

or three-directional cloaking by exploiting the symmetry of the entire system based on the configurations that have been developed thus far. Moreover, the experiments implemented in this thesis do not constitute a direct demonstration of macroscopic cloaking and hence much improvement is still required in future research to demonstrate this achievement in a canonical fashion.

Appendix A

List of Abbreviations

CV	**cylindrical vetor**
PSF	**point spread function**
AR	**anti-resolution**
NA	**numerical aperture**
BOE	**binary optical element**
DOE	**diffraction optical element**
DOF	**depth of focus**
SLM	**spatial light modulator**

Appendix B

List of Publications

1. **Chao Wan**, Kun Huang, Tiancheng Han, Eunice S. P. Leong, Weiqiang Ding, Lei Zhang, Tat-Soon Yeo, Xia Yu, Jinghua Teng, Dang Yuan Lei, Stefan A. Maier, Boris Luk'yanchuk, Shuang Zhang and Cheng-Wei Qiu, "Three-dimensional visible light capsule enclosing perfect super-sized darkness via anti-resolution", *Laser Photonics Rev.*, 1-7 (2014). Supporting Information: http://dx.doi.org/10.1002/lpor.201400006

2. Huapeng Ye, **Chao Wan**, Kun Huang, Tiancheng Han, Jinghua Teng, Yeo Swee Ping, and Cheng-Wei Qiu1, "Creation of vectorial bottle-hollow beam usingradially or azimuthally polarized light", *Opt. Lett.* 39, 630-633 (2014).

Bibliography

[1] Y. R. Shen, *The principles of nonlinear optics*. New York, Wiley-Interscience, 1984.

[2] K. Shimoda, *Introduction to laser physics*. Berlin and New York, Springer-Verlag, 1984.

[3] H. P. Herzig, *Micro-optics: elements, systems and applications*, CRC Press, 2012.

[4] C. Hnatovsky, V. Shvedov, W. Krolikowski, and A. Rode, "Revealing Local Field Structure of Focused Ultrashort Pulses", *Phys. Rev. Lett.* 106, 123901 (2011).

[5] Q. Zhan, "Cylindrical vector beams: from mathematical concepts to applications," *Adv. Opt. Photon.* 1, 1-57 (2009).

[6] D. Pohl, "Operation of a Ruby laser in the purely transverse electric mode TE01," *Appl. Phys. Lett*. 20, 266-267 (1972).

[7] Y. Mushiake, K. Matzumurra, and N. Nakajima, "Generation of radially polarized optical beam mode by laser oscillation," *Proc. IEEE*

60, 1107-1109 (1972).

[8] S. Quabis, R. Dorn, M. Eberler, O. Glöckl, and G. Leuchs, "Focusing light into a tighter spot," *Opt. Commun.* 179, 1-7 (2000).

[9] R. Dorn, S. Quabis, and G. Leuchs, "Sharper focus for a radially polarized light beam," *Phys. Rev. Lett*. 91, 233901 (2003).

[10] B. Jia, X. Gan, and M. Gu, "Direct measurement of a radially polarized focused evanescent field facilitated by a single LCD," *Opt. Express* 13, 6821-6827 (2005).

[11] B. Hao and J. Leger, "Experimental measurement of longitudinal component in the vicinity of focused radially polarized beam," *Opt. Express* 15, 3550-3556 (2007).

[12] Q. Zhan and James R. Leger, "Focus shaping using cylindrical vector beams," *Opt. Express* 10, 324-331 (2002).

[13] L. Novotny, M.R. Beversluis, K. S. Youngworth, and T. G. Brown, "Longitudinal Field Modes Probed by Single Molecules," *Phys. Rev. Lett*. 86, 5251 (2001).

[14] M. O. Scully, "A simple laser linac," *Appl. Phys. B* 51, 238 (1990).

[15] Y. Q. Zhao, Q. Zhan, Y. L. Zhang, and Y. P. Li, "Creation of a three-dimensional optical chain for controllable particle delivery," *Opt. Lett*. 30, 848-850 (2005).

[16] Yuichi Kozawa and Shunichi Sato, "Focusing property of a double-ring-shaped radially polarized beam," *Opt. Lett*. 31, 820-822

(2005).

[17] J. Wang, W. Chen, and Q. Zhan, "Engineering of high purity ultra-long optical needle field through reversing the electric dipole array radiation," *Opt. Express* 18, 21965-21972 (2010).

[18] N. Fang, H. Lee, C. Sun, and X. Zhang, "Sub-diffraction-limited optical imaging with a silver superlens," *Science* 308, 534-537 (2005).

[19] Z. W. Liu, H. Lee, Y. Xiong, C. Sun, and X. Zhang, "Far-field optical hyperlens magnifying sub-diffraction-limited objects," *Science* 315, 1686-1686 (2007).

[20] K. I. Willig, S. O. Rizzoli, V. Westphal, R. Jahn, S. W. Hell, "STED microscopy reveals that synaptotagmin remains clustered after synaptic vesicle exocytosis," *Nature* 440, 935 (2006).

[21] S. Van de Linde, A. Loschberger, T. Klei, M. Heidbreder, S. Wolter, M. Heilemann, M. Sauer, "Direct stochastic optical reconstruction microscopy with standard fluorescent probes," *Nature Photon*. 6, 991 (2011).

[22] M. Born, E. Wolf, *Principles of Optics*, Cambridge University Press, Cambridge (1999).

[23] C. S. Williams and O. A. Becklund, *Introduction to the optical transfer function*. New York: Wiley (1989).

[24] E. Wolf, "Electromagnetic diffraction in optical systems I: An integral representation of the image field," *Proc. R. Soc. Lond. A* 253, 349-357

(1959).

[25] B. Richards and E. Wolf, "Electromagnetic diffraction in optical systems II: Structure of the image field in an aplanatic system," *Proc. R. Soc. Lond. A* 253, 358-379 (1959).

[26] J. B. Pendry, D. Schurig, and D. R. Smith. "Controlling electromagnetic fields," *Science* 312, 1780-1782 (2006).

[27] J. A. Stratton, *Electromagnetic Theory*. New York: McGraw-Hill, 1941.

[28] R. F. Harrington, *Time-Harmonic Electromagnetic Fields*. New York: McGraw-Hill, 1961.

[29] J. D. Jackson, *Classical Electrodynamics*. New York: Wiley, 1975.

[30] J. D. Kraus, *Electromagnetics*. New York: McGraw-Hill, 1973.

[31] Q. Wang, G. D. Li, and K. Gong, *Electromagnetics theory foundations*. Tsinghua University Press, 2001.

[32] J. J. Mao and J. G. He, *Electromagnetics field theory*. National University of Defense Technology Press, 1998.

[33] J. A. Kong, *Electromagnetic waves theory*. John Wiley and Sons, Inc., 1986.

[34] J. M. J, *The Finite Element Method in Electromagnetics*. John Wiley and Sons, Inc., 2002.

[35] D. G. Hall, "Vector-beam solutions of Maxwell's wave equation," *Opt. Lett.* 21, 9-11 (1996).

[36] R. H. Jordan and D. G. Hall, "Free-space azimuthal paraxial wave equation: the azimuthal Bessel-Gauss beam solution," *Opt. Lett.* 19, 427-429 (1994).

[37] K. Huang, P. Shi, G. W. Cao, K. Li, X. B. Zhang, and Y. P. Li. "Vector-vortex Bessel-Gauss beams and their tightly focusing properties," *Opt. Lett.* 36, 888-890 (2011).

[38] C. F. Li, "Integral transformation solution of free-space cylindrical vector beams and prediction of modified Bessel-Gaussian vector beams," *Opt. Lett.* 32, 3543-3545 (2007).

[39] C. F. Li, "Unified theory for Goos-Hänchen and Imbert-Fedorov effect", *Phys. Rev. A* 76, 013811 (2007).

[40] Kun Huang, *Vector Singular Beams' Properties of Propagation, Tightly Focusing and its Applications*, PhD thesis, University of Science and Technology of China, China, 2012.

[41] G. B. Airy, *Trans. Camb. Phil. Soc.* 5, 271-280 (1834).

[42] J. J. M. Braat, S. van Haver, A. J. E. M. Janssen, and P. Dirksen, "Assessment of optical systems by means of point-spread functions," *Progress in Optics*, vol. 51, 349-468 (2008).

[43] A. S. van de Nes, *Rigorous Electromagnetic Field Calculations for Advanced Optical Systems*, PhD thesis, Delft University of Technology, 2005.

[44] P. Debye, *Ann. Phys. Lpz*. 30, 755 (1909).

[45] E. Wolf and Y. J. Li, “Conditions for the validity of the Debye integral representation of focused fields,” *Opt. Commun.* 39, 205-210 (1981).

[46] K. S. Youngworth and T. G. Brown, “Focusing of high numerical aperture cylindrical-vector beams,” *Opt. Express* 7, 77-87 (2000).

[47] Rayleigh, *Phil. Mag*. 8, 403 (1879).

[48] E. Wolf, “The diffraction theory of aberrations,” *Rep. Prog. Phys.* 14, 95-120 (1951).

[49] Lommel, E., *Abh. Bayer. Akad.* 15 (2), 233 (1885); *Abh. Bayer. Akad.* 15 (3) 531 (1886).

[50] Strehl, K., *Theorie des Fernrohrs*, Barth, Leipzig (1894).

[51] B. R. A. Nijboer, *The diffraction theory of Aberrations*, PhD thesis, 1942.

[52] V. S. Ignatowsky, "Diffraction by a lens of arbitrary aperture," *Tr. Opt. Inst.* 1 (4), 1 (1919).

[53] H. H. Hopkins, “The airy disc formula for systems of high relative aperture,” *Proc. Phys. Soc.* 55, 116 (1943).

[54] J. B. Pendry, “Negative refraction makes a perfect lens,” *Phys. Rev. Lett.* 85, 3966-3969 (2000).

[55] T. Taubner, D. Korobkin, Y. Urzhumov, G. Shvets, and R. Hillenbrand, “Near-field microscopy through a SiC superlens,” *Science* 313, 1595-1595 (2006).

[56] I. I. Smolyaninov, Y. J. Huang, and C. C. Davis, “Magnifying

superlens in the visible frequency range," *Science* 315, 1699-1701 (2007).

[57] X. Zhang and Z. Liu, "Superlenses to overcome the diffraction limit," *Nature Mater.* 7, 435-441 (2008).

[58] D. Lu and Z. W. Liu, "Hyperlenses and metalenses for far-field super-resolution imaging," *Nature Commun.* 3, 1205 (2012).

[59] F. M. Huang and N. I. Zheludev, "Super-resolution without evanescent waves," *Nano Lett.* 9, 1249-1254 (2009).

[60] E. T. F. Rogers, J. Lindberg, T. Roy, S. Savo, J. E. Chad, M. R. Dennis, and N. I. Zheludev, "A super-oscillatory lens optical microscope for subwavelength imaging," *Nature Mater.* 11, 432-435 (2012).

[61] J. Rho, Z. L. Ye, Y. Xiong, X. B. Yin, Z. W. Liu, H. Choi, G. Bartal, and X. Zhang, "Spherical hyperlens for two-dimensional sub-diffractional imaging at visible frequencies," *Nature Commun.* 1, 143 (2010).

[62] J. J. M. Braat, P. Dirksen, A. J. E. M. Janssen, S. van Haver, and A. S. van de Nes, "Extended Nijboer-Zernike approach to aberration and birefringence retrieval in a high-numerical-aperture optical system," *J. Opt. Soc. Am. A* 22, 2635-2650 (2005).

[63] A. J. E. M. Janssen, S. van Haver, P. Dirksen, and J. J. M. Braat, "Zernike representation and Strehl ratio of optical systems with variable numerical aperture," *J. Mod. Opt.* 55, 1127-1157 (2008).

[64] S. van Haver, J. J. M. Braat, A. J. E. M. Janssen, O. T. A. Janssen, and S. F. Pereira, "Vectorial aerial-image computations of three-dimensional objects based on the Extended Nijboer-Zernike theory," *J. Opt. Soc. Am. A* 26, 1221-1234 (2009).

[65] S. van Haver, *Extended Nijboer-Zernike diffraction and aberration retrieval theory for high-numerical-aperture optical imaging systems*, Master's thesis, Delft University of Technology, 2005.

[66] S. van Haver, *The Extended Nijboer-Zernike diffraction and its applications*, PhD thesis, Delft University of Technology, 2010.

[67] J. J. M. Braat, P. Dirksen, A. J. E. M. Janssen, and A.S. van de Nes, "Extended Nijboer-Zernike representation of the vector field in the focal region of an aberrated high-aperture optical system," *J. Opt. Soc. Am. A* 20, 2281-2292 (2003).

[68] A. S. van de Nes, L. Billy, S. F. Pereira, and J. J. M. Braat, "Calculation of the vectorial field distribution in a stratified focal region of a high numerical aperture imaging system," *Opt. Express* 12, 1281-1293 (2004).

[69] H. Wang, L. Shi, B. Lukyanchuk, C. Sheppard, and C. T. Chong, "Creation of a needle of longitudinally polarized light in vacuum using binary optics," *Nature Photon.* 2, 501-505 (2008).

[70] J. Durnin, J. J. Miceli, Jr., and J. H. Eberly, "Diffraction free beams," *Phys. Rev. Lett.* 58, 1499-1501 (1987).

[71] J. Durnin, "Exact solutions for nondiffracting beams. I. The scalar theory," *J. Opt. Soc. Am. A* 4, 651-654 (1987).

[72] R. M. Herman and T. A. Wiggins, "Production and uses of diffractionless beams," *J. Opt. Soc. Am. A* 8, 932-942 (1991).

[73] A. VaARa, J. Turunen, and A. T. Friberg, "Realization of general nondiffracting beams with computer-generated holograms," *J. Opt. Soc. Am. A* 6, 1748-1754 (1989).

[74] P. L. Overfelt and C. S. Kenney, "Comparison of the propagation characteristics of Bessel, Bessel–Gauss, and Gaussian beams diffracted by a circular aperture," *J. Opt. Soc. Am. A* 8, 732-945 (1991).

[75] W. X. Cong, N. X. Chen, and B. Y. Gu, "Generation of nondiffracting beams by diffractive phase elements," *J. Opt. Soc. Am. A* 15, 2362-2364 (1998).

[76] G. Indebetouw, "Nondiffracting optical fields: some remarks on their analysis and synthesis," *J. Opt. Soc. Am. A* 6, 150-152 (1989).

[77] P. Szwaykowski and J. Ojeda-Castaneda, "Nondiffracting beams and the self-imaging phenomenon," *Opt. Commun.* 83, 1–4 (1991).

[78] K. Thewes, M. A. Karim, and A. A. S. Awwal, "Diffraction free beam generation using refracting systems," *Opt. Laser Technol.* 23, 105–108 (1991).

[79] Z. Bouchal, J. Bajer, and M. Bertolotti, "Vectorial spectral analysis of the nonstationary electromagnetic field," *J. Opt. Soc. Am. A* 15,

2172-2181 (1998).

[80] J. Fagerholm, A. T. Friberg, D. P. Morgan, and M. Salomaa, "Angular-spectrum representation of nondiffracting X waves," *Phys. Rev. E* 54, 4347–4352 (1996).

[81] A. T. Friberg, J. Fagerholm, and M. Salomaa, "Spacefrequency analysis of nondiffracting pulses," *Opt. Commun.* 136, 207-212 (1997).

[82] Z. Bouchal, "Nondiffractiong optical beams: physical properties, experiments, and applications," *Czech. J. Phys.* Vol. 53 (2003).

[83] D. Ding and X. Liu, "Approximate description for Bessel, Bessel–Gauss, and Gaussian beams with finite aperture," *J. Opt. Soc. Am. A* 16, 1286–1293 (1999).

[84] F. Gori, G. Guattari, and C. Padovani, "Bessel–Gauss beams," *Opt. Commun.* 64, 491-495 (1987).

[85] Z. Bouchal, "Controlled spatial shaping of nondiffracting patterns and arrays," *Opt. Lett*. 27, 1376-1378 (2002).

[86] S. Ruschin, "Modified Bessel nondiffracting beams," *J. Opt. Soc. Am. A* 11, 3224-3228 (1994).

[87] S. Ruschin and A. Leizer, "Evanescent Bessel beams," *J. Opt. Soc. Am. A* 15, 1139-1143 (1998).

[88] J. Perczel, T. Tyc, and U. Leonhardt, "Invisibility cloaking without superluminal propagation," *New J. Phys*. 13, 083007 (2011).

[89] J. Courtial, "Self-imaging beams and the Guoy effect," *Optics Comm.* 151, 1-4 (1998).

[90] Min Gu, *Advanced optical imaging theory*, 75 Springer-Verlag, New York (1999).

[91] K. Huang, P. Ye, J. H. Teng, Swee Ping Yeo, Boris Luk'yanchuk and Cheng-Wei Qiu1, "Optimization-free super-oscillatory lens using amplitude and phase masks", *Laser Photonics Rev.,* 8, 152-157 (2014).

[92] J. E. Dennis, R.B. Schnabel, *Numerical methods for unconstrained optimization and nonlinear equations*, New Jersey: Pretice-Hall, 1983.

[93] J. Nocedal and S. J. Wright, *Numerical Optimization*, 2nd edition, Springer, 2006.

[94] U. Leonhardt. "Optical conformal mapping," *Science* 312 1777-1780 (2006).

[95] H. Y. Chen, B. Hou, S. Y. Chen, X. Y. Ao, W. J. Wen, and C. T. Chan, "Design and experimental realization of a broadband transformation media field rotator at microwave frequencies," *Phys. Rev. Lett.* 102, 183903 (2009).

[96] Y. Luo, J. J. Zhang, H. S. Chen, J. Tao, H. Fu, and L. X. Ran, "High-directivity antenna with small antenna aperture," *Appl. Phys. Lett.* 95, 193506 (2009).

[97] V. M. Shalaev, "Transforming light," *Science* 322, 384-386 (2008).

[98] D. Schurig, J. B. Pendry, and D. R. Smith, "Calculation of material

properties and ray tracing in transformation media," *Opt. Express* 14, 9794-9804 (2006).

[99] H. S. Chen, B. -I. Wu, B. L. Zhang, and J. A. Kong, "Electromagnetic wave interactions with a metamaterial cloak," *Phys. Rev. Lett.* 99, 063903 (2007).

[100] S. A. Cummer, B. -I. Popa, D. Schurig, D. R. Smith, and J. Pendry, "Full-wave simulations of electromagnetic cloaking structures," *Phys. Rev. E* 74, 036621 (2006).

[101] D. Schurig, J. J. Mock, B. J. Justice, S. A. Cummer, J. B. Pendry, A. F. Starr, and D. R. Smith, "Metamaterial electromagnetic cloak at microwave frequencies," *Science* 314, 977-980 (2006).

[102] W. S. Cai, U. K. Chettiar, A. V. Kildishev, and V. M. Shalaev, "Optical cloaking with metamaterials," *Nature Photon.* 1, 224-227 (2007).

[103] Z. Ruan, M. Yan, C. W. Neff, and M. Qiu, "Ideal cylindrical cloak: Perfect but sensitive to tiny perturbations," *Phys. Rev. Lett.* 99, 113903 (2007).

[104] Z. Liang, P. Yao, X. Sun, and X. Jiang, "The physical picture and the essential elements of the dynamical process for dispersive cloaking structures," *Appl. Phys. Lett.* 92, 131118 (2008).

[105] W. Yan, M. Yan, and M. Qiu, "Non-magnetic simplified cylindrical cloak with suppressed zeroth order scattering," *Appl. Phys. Lett.* 93,

021909 (2008).

[106] A. V. Kildishev, W. Cai, U. K. Chettiar, and V. M. Shalaev, "Transformation optics: approaching broadband electromagnetic cloaking," *New journal of Physics* 10, 115029 (2008).

[107] H. Y. Chen, Z. X. Liang, P. J. Yao, X. Y. Jiang, H. R. Ma, and C. T. Chan, "Extending the bandwidth of electromagnetic cloaks," *Phys. Rev. B* 76, 241104 (2007).

[108] A. Alu and N. Engheta, "Cloaked near-field scanning optical microscope tip for noninvasive near-field imaging," *Phys. Rev. Lett.* 105, 263906 (2010).

[109] H. Y. Chen and C. T. Chan, "Acoustic cloaking in three dimensions using acoustic metamaterials," *Appl. Phys. Lett.* 91, 183518 (2007).

[110] M. Farhat, S. Guenneau, and S. Enoch, "Ultrabroadband Elastic Cloaking in Thin Plates," *Phys. Rev. Lett.* 103, 024301 (2009).

[111] S. Zhang, D. A. Genov, C. Sun, and X. Zhang, "Cloaking of matter waves," *Phys. Rev. Lett.* 100, 123002 (2008).

[112] J. Li and J. B. Pendry, "Hiding under the Carpet: A New Strategy for Cloaking," *Phys. Rev. Lett.* 101, 203901 (2008).

[113] R. Liu, C. Ji, J. J. Mock, J. Y. Chin, T. J. Cui, and D. R. Smith, "Broadband ground-plane cloak," *Science* 323, 366-369 (2009).

[114] H. F. Ma and T. J. Cui. "Three-dimensional broadband ground-plane cloak made of metamaterials," *Nature Commun.* 1, 21 (2010).

[115] J. H. Lee, J. Blair, V. A. Tamma, Q. Wu, S. J. Rhee, C. J. Summers, and W. Park, "Direct visualization of optical frequency invisibility cloak based on silicon nanorod array," *Opt. Express* 17 12922-12928 (2009).

[116] J. Valentine, J. Li, T. Zentgraf, G. Bartal, and X. Zhang, "An optical cloak made of dielectrics," *Nature Materials* 8, 568-571 (2009).

[117] T. Ergin, N. Stenger, P. Brenner, J. B. Pendry, and M. Wegener, "Three-Dimensional Invisibility Cloak at Optical Wavelengths," *Science* 328, 337-339 (2010).

[118] B. L. Zhang, T. Chan, and B.-I. Wu, "Lateral Shift Makes a Ground-Plane Cloak Detectable," *Phys. Rev. Lett.* 104, 233903 (2010).

[119] X. Z. Chen, Y. Luo, J. J. Zhang, K. Jiang, J. B. Pendry, and S. Zhang, "Macroscopic invisibility cloaking of visible light," *Nature Commun.* 2, 176 (2011).

[120] B. L. Zhang, Y. Luo, X. G. Liu, and G. Barbastathis, "Macroscopic Invisibility Cloak for Visible Light," *Phys. Rev. Lett.* 106, 033901 (2011).

[121] H. Chen and B. Zheng. "Broadband polygonal invisibility cloak for visible light," *Scientific Reports* 2, 255 (2012).

[122] T. C. Han, *Theoretical Study of Novel Electromagnetic Devices Based on Transformation Optics*, PhD thesis, University of Electronic Science and Technology of China, China, 2012.

[123] J. T. Foley and E. Wolf, "Wave-front spacing in the focal region of high-numerical-aperture systems," *Opt. Lett.* 30, 1312-1314 (2005).

[124] T. D. Visser and J. T. Foley, "On the wavefront spacing of focused, radially polarized beams," *J. Opt. Soc. Am. A* 22, 2527-2531 (2005).

[125] A. Minovich, A. E. Klein, N. Janunts, T. Pertsch, D. N. Neshev, and Y. S. Kivshar, "Generation and Near-Field Imaging of Airy Surface Plasmons," *Phys. Rev. Lett.* 107, 116802 (2011).

[126] P. Zhang, S. Wang, Y. M. Liu, X. B. Yin, C. G. Lu, Z. G. Chen, and X. Zhang, "Plasmonic Airy beams with dynamically controlled trajectories," *Opt. Lett.* 36, 3191-3193 (2011).

[127] K. T. Gahagan and G. A. Swartzlander, Jr., "Optical vortex trapping of particles," *Opt. Lett.* 21, 827-829 (1996).

[128] J. Arlt and M. J. Padgett, "Generation of a beam with a dark focus surrounded by regions of higher intensity: the optical bottle beam," *Opt. Lett.* 21, 191-193 (2000).